Intrinsic Capacitance, Charge Storage Mechanisms, and Defect Engineering of Molybdenum Disulfide Nanosheets

by

Jialu Chen

A thesis

presented to the University of Waterloo

in fulfillment of the

thesis requirement for the degree of

Master of Applied Science

in

Chemical Engineering (Nanotechnology)

Waterloo, Ontario, Canada, 2020

Author's Declaration

I hereby declare that I am the sole author of this thesis. This is a true copy of the thesis, including any required final revisions, as accepted by my examiners.

I understand that my thesis may be made electronically available to the public.

Abstract

Single layer 2D materials such as the metallic, 1T polymorph of molybdenum disulfide (MoS_2) hold significant promise for next-generation supercapacitors due to their high theoretical surface area and ability to be assembled into electrodes with high bulk density boosting volumetric capacitance. While significant research has emerged in the last few years devoted to MoS_2 and graphene-MoS_2 hybrid electrode systems, little is known regarding fundamental double-layer charging mechanisms in this system. In this work, we determine the potential and frequency dependent area-specific double-layer capacitance of the electrode/electrolyte interface using the 1T and 2H polymorphs of MoS_2. Furthermore, we aim to understand restacking effects and possible intercalation mechanisms in multilayer MoS_2 films, as well as how the intrinsic capacitance can be enhanced by defect engineering.

To by-pass the challenges and uncertainties associated with porous electrodes, we carry out measurements on non-porous monolayer electrodes supported by atomically flat graphite single crystals. Monolayer films were prepared by using a variation of the Langmuir Blodgett deposition method to create films of chemically exfoliated molybdenum disulfide (MoS_2) and chemically reduced graphene oxide (rGO) using a recently developed barrier-free densification method. The films were characterized to determine surface coverage, surface roughness, layer number and electrode material chemistry. The frequency and voltage-dependent capacitance of monolayer, bilayer, and trilayer films were measured by cyclic voltammetry and impedance spectroscopy.

The results demonstrate that the metallic 1T polymorph of MoS_2 ($C_{a,1T}$ = 14.9 µF/cm^2) has over tenfold the capacitance of the semiconducting 2H polymorph ($C_{a,2H}$ = 1.35 µF/cm^2) near the open circuit potential and under negative polarization in aqueous electrolyte. However, under positive polarization the capacitance is significantly reduced and behaves similarly to the 2H polymorph. While the capacitance of rGO films does not increase with increasing layer number, the capacitance of 1T-MoS_2 films scaled with layer number, even at high frequency, suggesting easy and rapid ion intercalation between the restacked sheets. The results of these studies allow us to determine the limiting factors and upper limits of capacitance expected from MoS_2 composites and provides engineering design criteria for building higher performance MoS_2 composite electrodes.

Furthermore, in order to extend the potential upper capacitance limits of MoS_2 supercapacitors, defect engineering is explored in MoS_2 nanosheet films. Two types of defects are introduced into MoS_2: sulfur vacancies and edge sites. Sulfur vacancies are created by increasing the amount of lithium intercalant used while edge sites are produced simply by decreasing the lateral size of MoS_2 nanosheets through sonication. When transitioning from 0% to 6.6% sulfur vacancies, the intrinsic capacitance increases consistently. Conversely, while decreasing flake size by 40 nm increases the measured capacitance, further size reduction by 80 nm results in decreased capacitance. These results demonstrate that defect engineering through careful tuning of MoS_2 nanosheet synthesis allows for considerable improvements to the intrinsic capacitance.

Acknowledgements

I would like to first thank my supervisor, Dr. Michael. A. Pope, for his guidance during my Master's studies. His insight, passion, and patience were instrumental in the completion of my thesis. Thank you for helping me through hardships and inspiring my breakthroughs. I could not have done this without you.

As for the rest of the people in this wonderful group, I would like to acknowledge every single one of you. I'm so grateful for the chance to work with you and wish you all the best in your futures. In particular, I would like to thank Amanda Xu, Andy She, and Mariam Gad for their continued support during my studies.

I would also like to thank Dr. Mark Prtizker and Dr. Rodney Smith for being on my committee. I would again like to thank Dr. Juewen Liu for letting me use his Zetasizer instrument. I would also like to thank Mr. Wesley Walker and Ms. Olga Krysiak for their contributions in our collaborations.

Finally, I'd like to thank my parents for their unconditional, unwavering love all these years. We've been through so much as a family, but you've always been by my side, making sure I knew how proud you were. Last, but not least, I would like to thank Theeran for being there for me, every step of the way. Loving me isn't always easy, but you make it seem effortless.

Dedication

Dedicated to my family, friends, and the love of my life.

Table of Contents

List of Figures

List of Tables

List of Abbreviations

2DEG	Two dimensional electron gas
AFM	Atomic force microscopy
CV	Cyclic voltammetry
DCE	1,2-Dichloroethane
DLS	Dynamic light scattering
DMF	Dimethyl formamide
DOS	Density of states
EDS	Energy-dispersive X-ray spectroscopy
EIS	Electrochemical impedance spectroscopy
GO	Graphene oxide
HOPG	Highly ordered pyrolytic graphite
LB	Langmuir-Blodgett
LSSA	Langmuir specific surface area
PTFE	Polytetrafluorethylene
pzc	Point of zero charge
rGO	Reduced graphene oxide
SEM	Scanning electron microscopy
TMD	Transition metal dichalcogenide
UV-Vis	Ultraviolet visible
XPS	X-ray photoelectron spectroscopy

C_a	Intrinsic capacitance
C_H	Helmholtz capacitance
C_{SC}	Space charge capacitance
C_{diff}	Diffuse double layer capacitance
C_{dl}	Double layer capacitance
C_Φ	Pseudocapacitance
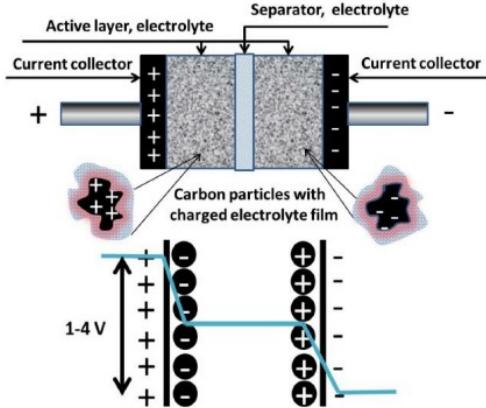
And when my time is up,
have I done enough?
Will they tell my story?

Chapter 1: Introduction

The negative environmental consequences of continuous fossil fuel usage include climate change,[1] the endangerment of eco-diversity,[2] and major environmental pollution.[1,3] Attempts to slow or reverse these impacts have motivated and inspired considerable advances in the field of renewable energy. Much focus has been placed on harnessing solar, wind, and hydro energy sources, but their intermittent nature complicates their integration into our current electric power system.[1,3] Typically, these types of energy sources cannot continuously generate electricity and instead, provide substantial amounts of energy on a relatively short time scale. Therefore, the development of suitable energy storage systems is of equal importance as the development of energy generation systems.[3]
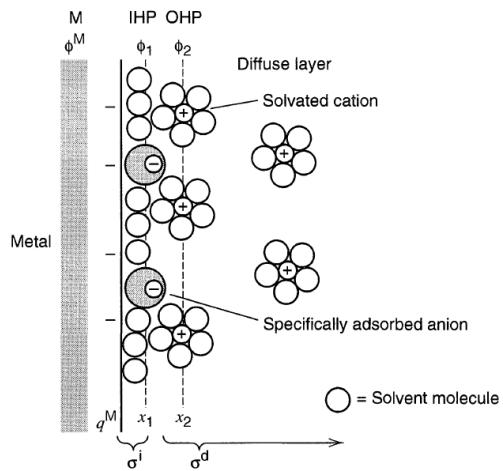
Currently, lithium ion batteries have been employed as the conventional storage device for renewable energy sources, but while their capacity is impressive, they are limited by slow charging rates and poor cycle life.[4-7] Supercapacitors are an interesting alternative energy storage device to the lithium ion battery which can demonstrate remarkable power density and charge/discharge stability.[4-7] They consist of two porous, high surface area electrodes laminated onto current collectors, the pore-space filled with solid state or liquid electrolytes and electrically isolated by porous ionically conducting separators, as seen in Figure 1.[5,8]

Charge storage in a supercapacitor typically occurs through one of two pathways: electric double layer capacitance (C_{dl}) or pseudocapacitance (C_Φ). C_{dl} charging takes place when an electric potential is applied, resulting in an electric field that induces ion rearrangement at the electrode/electrolyte interface and a sub-nanometer separation of charge, as shown in Figure 2.

Figure 1. Schematic structure of a single cell supercapacitor. (Reproduced from ref. 3)

The double layer consists of 3 primary phases. The inner Helmholtz plane (IHP) consists of ions that have lose their solvation shells and are in direct contact with the electrode. These are known as "specifically adsorbed ions." Meanwhile, the outer Helmholtz plane (OHP) consists of solvated ions which adsorb atop the IHP through Coulombic attraction. Finally, there is the diffuse layer, which extends past the OHP and is comprised of free ions. These ions traverse the fluid according to Coulombic attraction and Brownian motion, rather than being firmly anchored.[9,10]

Figure 2. Schematic diagram of the formation of the electric double layer. (Reproduced from ref. 3)

2

The double layer capacitance scales linearly with electrode surface area, similarly to parallel plate capacitance, according to the equation $C = \frac{\epsilon A}{d}$, where ϵ is the dielectric constant, A is the area of the plates, and d is the separation between plates.[10] Conversely, C_Φ charging involves faradaic processes between electrode and electrolyte.[10] These processes involve an electron charge transfer, either through reduction-oxidation reactions, electrosorption, or intercalation.[10] Despite higher energy densities, C_Φ charging is typically limited to lower rates due to the finite rate constants associated with such chemical reactions as well as poor reversibility compared to the purely electrostatic mechanism of double-layer charging. This typically results in poorer cycle stability and rate capability, rendering double layer capacitance a more compelling pathway.[3]

Supercapacitors have been shown to operate for thousands of charge/discharge cycles and have tenfold power density compared to lithium ion batteries, making them uniquely suited for use alongside renewable energy.[3] Their main downside is their comparatively lower energy density, which can be attributed to their storage mechanism.[3] Consequently, the development of suitable, high surface area electrode materials is of paramount importance when it comes to supercapacitor development.[3]

Nanomaterials, especially carbon-based nanomaterials such as graphene and molybdenum disulfide (MoS_2), have garnered considerable interest in this field as they offer a superior surface area to volume ratio.[1,3,8,11] MoS_2 is a layered transition metal dichalcogenide which has recently become a commonly used material in supercapacitor electrodes. Since it is a much denser material than graphene, it has potential to enable more space efficient devices.[1,3,12] However, while much research has been dedicated to the development of supercapacitor materials, comparatively little

focus has been placed on fundamental studies which explore how charge is stored within supercapacitor electrodes.

Therefore, in this work, I will present an investigation into the fundamental properties of MoS_2 as they relate to charge storage in supercapacitor devices, by examining monolayer MoS_2 nanosheets deposited onto non-porous, flat electrodes. Focus will be placed on the intrinsic capacitance, mechanisms of charge storage, and influence of defect engineering on capacitance performance. The overarching objective of this thesis is essentially to determine how to boost the energy density of MoS_2-based supercapacitors. This will be accomplished by investigating various fundamental phenomena concerning MoS_2 nanosheets and charge storage. Specifically, the intrinsic capacitance of the 1T and 2H polymorphs of MoS_2 will be probed for the first time, the effects of restacking on both MoS_2 and reduced graphene oxide (rGO) nanosheets will be examined, and methods of defect engineering to enhance capacitance will be explored. My main hypotheses are that:

1) 1T MoS_2 will demonstrate a considerably higher capacitance than 2H MoS_2. This is because while 1T MoS_2 is a metallic material, 2H MoS_2 is a semiconducting material.[13]

2) rGO will be limited by restacking effects while MoS_2 will be unaffected, largely because the interlayer spacing for graphene nanosheets is much smaller than that of MoS_2 nanosheets.[13,14]

3) The capacitance of the MoS_2 will increase steadily with the quantity of defects because they are high activity sites which can increase conductivity.[15]

Chapter 2: Background
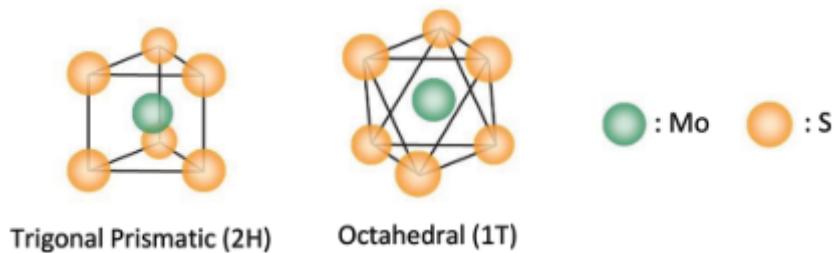
2.1 Supercapacitor Materials

Two-dimensional (2D) materials such as graphene or molybdenum disulfide (MoS_2) are compelling for use in next generation energy storage devices such as supercapacitors due to their potentially high ion-accessible surface areas, high conductivities and large electrochemical stability windows.[1,3,5] Since an electrode's capacitance is proportional to its specific ion-accessible surface area,[10] graphene remains one of the most promising electrode materials with 2630 m^2/g of potential surface area available for double-layer charging if each side of every sheet were accessible to the electrolyte ions in a thick, dense electrode.[16]

However, since graphene-based materials are known to re-stack during processing, only a small fraction of this surface area remains accessible. On the other hand, MoS_2 has a lower surface area (636 m^2/g),[17] but this is offset by a considerably higher density (5.36 g/cm^3 vs. 2.24 g/cm^3 for graphite), which leads to a potentially higher volumetric capacitance. The field was propelled forward by the discovery that ions could penetrate densely restacked MoS_2 structures resulting in some of the highest reported volumetric capacitances and energy densities of any material – even operating in high voltage-capable organic and ionic liquid-based electrolytes.[18] Consequentially, MoS_2 has been increasingly studied in supercapacitor research during the past few years.[1,3]
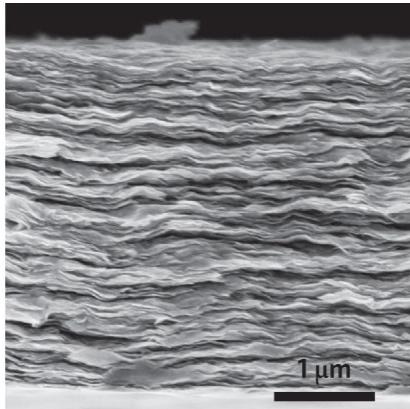
Molybdenum disulfide (MoS_2) is a layered transition metal dichalcogenide (TMD), which is typically found in nature as the semiconducting 2H phase, with trigonal prismatic coordination structure and hexagonal symmetry.[19] However, upon intercalation with alkali metals such as Li,

5

the metastable 1T phase is obtained.[20] Both phases are shown in Figure 3. This intercalation compound is exfoliated into single layers by adding it to water or other polar solvents which provides the basis for a process called chemical exfoliation[21] which is widely used to generate mixed 1T/2H MoS_2 single layers which can be converted back to 2H through various thermal[18,21] or solvothermal methods.[22] 1T MoS_2 is metallic, with octahedral coordination structure and tetragonal symmetry, and is 10^7 times more conductive than 2H MoS_2, which makes it a more compelling choice for use in supercapacitors.[18]

Trigonal Prismatic (2H)   Octahedral (1T)

Figure 3. Diagram of the 1T and 2H MoS_2 phases. (Reproduced from ref. 18.)

Acerce et al. were among the first to produce supercapacitor materials comprised solely of 1T MoS_2 by filtering suspensions of the material through membranes to restack the nanosheets into with thicknesses of up to 5 µm, as shown in Figure 4. This resulted in high volumetric capacitance values of ~400 to ~700 F/cm^3.[13] Since then, 1T MoS_2 has been incorporated into various types of morphologies, ranging from flower-like[23–26] to spherical[27–29] to foam-like,[30,31] either by itself as part of a composite.[12,32–36] While supercapacitor systems incorporating MoS_2 have been plentiful, fundamental studies of the material have been neglected. We are especially interested in the charge storage behaviour of MoS_2 when it comes to restacking.

6

Figure 4. SEM image of 1T MoS_2 supercapacitor cross-section. (Reproduced from ref. 13.)

Previously, it was shown that increasing graphene layers does not result in increased capacitance due to the way that the layers restack.[37] MoS_2 is thought to avoid such pitfalls through easier ion intercalation between the restacked layers.[18] Furthermore, unlike graphene[38–42] and graphite,[43–45] no studies of the intrinsic double-layer capacitance (C_a in $\mu F/cm^2$) of the MoS_2/electrolyte interface (1T or 2H, single layer or bulk) have been reported. This may be due, in part, to the unavailability of large enough single crystals of MoS_2 to be tested in an electrochemical cell – in contrast to highly oriented pyrolytic graphite (HOPG) which can be obtained in $\sim cm^2$ sizes that allowed for extensive electrochemical measurements on graphite's edge and basal-planes since the 1970s.[43,44]

2.2 Intrinsic Capacitance

The intrinsic capacitance of graphite and of graphene has been well-studied.[38–42,45,46] The early studies by Randin and Yeager on highly oriented pyrolytic graphite (HOPG) revealed an anomalously low capacitance of the basal-plane of graphite (3-4 $\mu F/cm^2$).[43,44] It was theorized that the double-layer capacitance was not dominated by the Helmholtz layer capacitance (C_H) of the electrolyte, as was known to be the case for a metal,[9] but dominated by a space charge capacitance

7

(C_{SC}) within the electrode itself. In addition to the diffuse layer capacitance (C_{diff}), the capacitances all add in series according to the following equation:

$$\frac{1}{C_a} = \frac{1}{C_{SC}} + \frac{1}{C_H} + \frac{1}{C_{diff}} \quad (1)$$
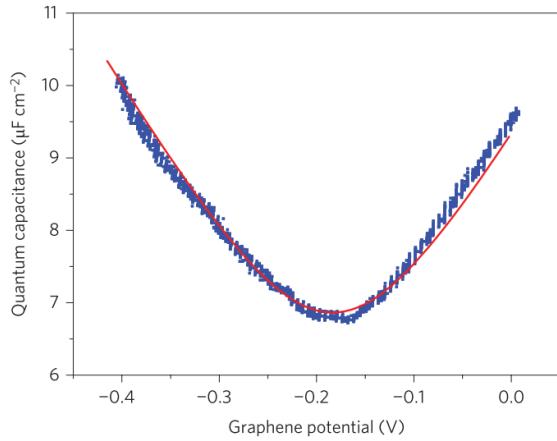
This was commonly observed for semiconductor electrodes[43,44] and was later, and more correctly, attributed to low density of electronic states near the Fermi energy for graphite which is a semimetal.[42] Since C_H is usually considerably larger than C_{SC}, C_a can often be approximated as C_{SC}. In pristine graphene, this effect manifests as what is termed a low space charge capacitance which has also been measured to be 3-4 $\mu F/cm^2$, behaving almost identically to HOPG, for graphene obtained by mechanical exfoliation[39] or chemical vapor deposition.[41]

Initial attempts to predict the double layer capacitance of graphite involved the assumption that it was a pure intrinsic semiconductor. C_{sc} was related to the charge carrier concentration (n): $C_{sc} = \left[\frac{2\varepsilon\varepsilon_0 e^2 n}{kT}\right]^{0.5} \cosh\left(\frac{\phi e}{2kT}\right)$, where φ is the surface potential, and k is Boltzmann's constant. The theory was refined by Gerischer, who theorized that graphite was not a semi-conductor, but a semi-metal, a material with a low density of states (DOS) near the Fermi level. He derived an expression relating C_{sc} of graphite to its density of states (N_0): $C_{sc} = \sqrt{\varepsilon\varepsilon_0 N_0 e}$, where ε and ε_0 represent the dielectric coefficient and constant, respectively.[45]

Alternate interpretations have then surfaced. Fang et al. modeled graphene as a two-dimensional, free-electron gas (2DEG) that was unable to fully screen the electric field created between two electrodes at different potentials. Due to a limited density of states, a quantum capacitance (C_Q) would be formed, and similarly added in series to C_H to form C_a. This C_Q was

then related to the carrier concentration (n): $C_Q \approx e^2 \frac{2}{\pi} \frac{eV_{ch}}{(\hbar v_F)} = \frac{2e^2}{\hbar v_F \sqrt{\pi}} \sqrt{n}$, where v_F is the Fermi

velocity, and $\hbar$ is the reduced Planck's constant.[39]

Since then, the 2DEG model for quantum capacitance has been adapted continuously,

whether to consider charge being stored on one or both sides of a graphene sheet or to incorporate

molecular dynamics and density functional theory.[41,47] On the experimental side, Xia et al. tested

the work of Fang et al. using a metal-oxide-semiconductor field-effect transistor (MOSFET).[39] As

shown in Figure 5, they found good agreement between the theoretical calculations (red) and their

measured values for quantum capacitance of graphene (blue).[39] The U-shaped voltage dependence

can be attributed to the existence of a Dirac point. At energies near the Fermi level, the valance

and conduction band take meet at certain points, taking the shape of the upper and lower halves

of a conical surface. At these Dirac points, both the density of states and quantum capacitance

are at a minimum.[39,48]

Figure 5. Quantum capacitance plotted against graphene potential for measured (blue) and calculated (red) values. (Reproduced from ref. 25)

It was also shown that a fourfold increase in intrinsic capacitance could be induced in graphene through the addition of functional groups and lattice defects, enabling graphene-based materials to act more like glassy carbon, a metallic form of carbon compared to graphene.[38,42] Only if all (defective) graphene surface area were exposed to the electrolyte would it be possible to achieve the often reported theoretical capacitance of 400-500 F/g, (~15-20 μF/cm$^2 \times$ 2630 m^2/g).[38]

C_a is an important metric that allows for more direct comparison between the charge storage capabilities of different supercapacitor electrode materials. However, the previously mentioned thick film electrodes are ill-suited for this purpose because of their porosity. In a porous system, C_a measurement requires estimations of accessible surface area, but it is not well understood which pores contribute to double layer charging.[38] Furthermore, the C_a is greatly affected by the electrode morphology. To illustrate, multilayer graphene has shown greater mass specific capacitance than monolayer graphene due to overlap of high capacitance edge-plane sites.[44,49] To circumvent such issues, fundamental studies of double layer charging can be carried out on polished, flat electrodes.[38,42]
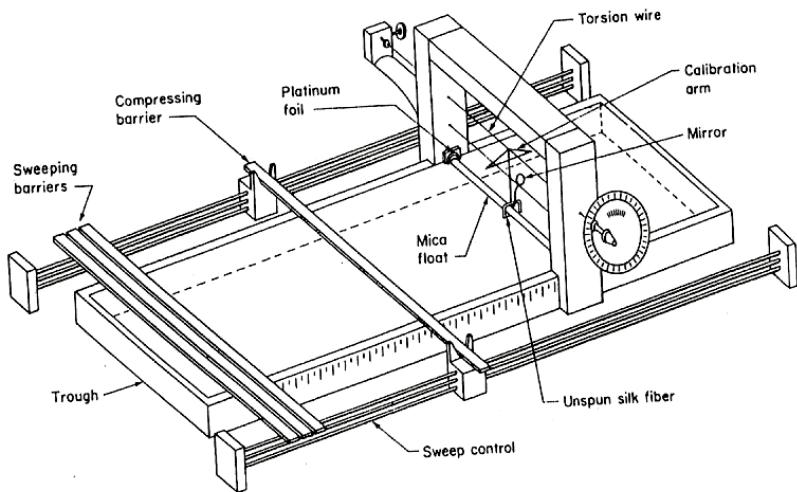
In a previous report, Pope et al. proposed a method to characterize electrochemical properties such as the double layer capacitance of graphene sheets without dealing with morphology and device related uncertainties.[42,50] Measurements were conducted on flat electrodes by depositing single layer coatings of densely tiled graphene onto pyrolytic graphite substrates using a modified Langmuir-Blodgett deposition method. A spring-loaded electrochemical cell allowed for the area-controlled capacitance measurements.

2.3 The Langmuir-Blodgett Technique

The first discovery towards the development of the Langmuir-Blodgett was made by Benjamin Franklin. In 1773, Franklin dropped a teaspoon of oil onto a pond, and noticed that the waves were instantly calmed for about half an acre. Though he did not know it, Franklin had created a monolayer of oil on the water's surface.[51]

More than a century later, Lord Rayleigh took a more quantitative approach to Franklin's experiment. He used the volume of oil dropped and area of coverage to calculate that the thickness of the film was 1.6 nm, the thickness of a molecule. Upon reading about his discovery in *Nature*, Agnes Pockels wrote a letter to Rayleigh, describing similar experiments that she had carried out in her kitchen sink. Using an earlier version of what would later be known as a Langmuir-Blodgett trough, shown in Figure 6, she was able to both produce monolayer films and measure their surface tension. From these experiments, she deduced that barriers could be used to control film area and that surface tension varied with the contaminant concentration.[51-53] Since she was "not in a position to publish [her] observations in scientific periodicals," Rayleigh forwarded her letter to *Nature*, where it was eventually published.[53]
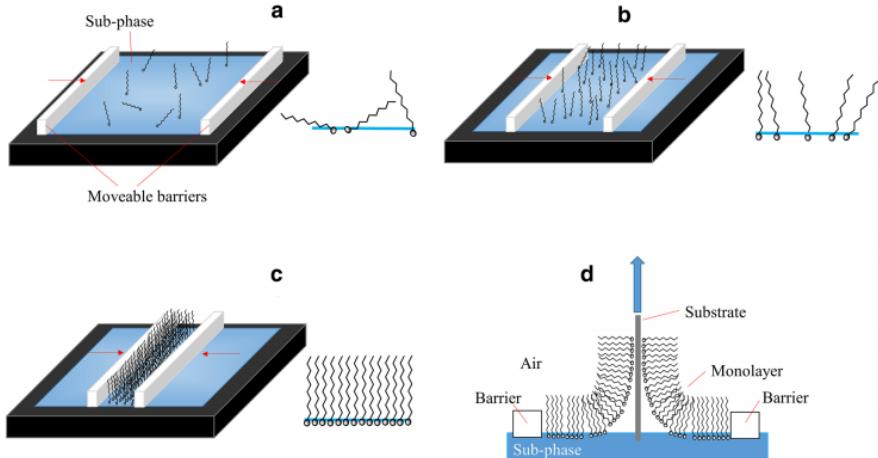
Irving Langmuir would later expand upon Pockels' initial experiments by explaining the mechanism behind the oil film formation. He theorized that certain oils were amphiphilic compounds that contained a water-soluble, hydrophilic head and an oil-soluble, oleophilic tail. Therefore, when the oil contacted the air-water interface, the hydrophilic heads would readily interact with the water while the hydrophobic tails would prefer the air phase.

Figure 6. Schematic diagram of a Langmuir-Blodgett trough. (Reproduced from ref. 38)

Using the known volume and area of the oil, the film thickness could be calculated, allowing for early investigations of molecular configuration. Langmuir's work in 1917 would garner him the 1932 Nobel Prize in chemistry.[51,54]

In the following years, Langmuir collaborated with Katharine Blodgett to develop a technique in which monolayer and multilayer films could be deposited onto water, metal, or glass. This technique, known as the Langmuir-Blodgett assembly, allowed for surface pressure monitoring alongside film deposition. A schematic diagram of the deposition process can be seen in Figure 7.[51,55] In the first step of the process, as seen in Figure 7a, amphiphilic compounds are introduced to the surface of the water, demonstrating no intermolecular interactions. In Figure 7b, the barriers are compressed such that molecules begin to interact with each other. Eventually, compression causes the molecules to self-assemble into a monolayer, as seen in Figure 7c. Through vertical deposition, as shown in Figure 7d, the monolayer can be transferred onto a solid substrate. This process can be repeated to form a multilayer film.[51,55]

12

Figure 7. Schematic diagram of a Langmuir-Blodgett film deposition. (Reproduced from ref. 42)

2.4 Motivation for the Project

Previous studies of intrinsic capacitance highlight the importance of research into intrinsic capacitance, as variations to theory or experimental design can result in vastly different predicted or measured quantities. Furthermore, since a more precise understanding of material performance enables the design of better supercapacitors, the intrinsic capacitance of MoS_2 is also of interest. Electron transport and quantum capacitance in MoS_2 have been studied in field-effect transistor (FET) devices. However, since the MoS_2 is typically placed atop a silicon oxide gate dielectric before being connected to source and drain, the oxide capacitance dominates all measurements.[56] Such a configuration does not allow for simple isolation of the intrinsic capacitance.[39] Furthermore, such studies did not account for the effects of morphology, 1T/2H ratio, or layer number on capacitance measurements and therefore cannot provide an accurate picture of the intrinsic capacitance of MoS_2. To circumvent such issues, this work involves the measurement of a single, densely packed MoS_2 monolayer on flat graphite single crystal substrates.

13

Since 1T MoS$_2$ is also a semimetal, its intrinsic capacitance may also be limited by electronic properties rather than by the electrolyte. Furthermore, the relatively large bandgap of 2H MoS$_2$ (~1.9 eV for a single layer) make it almost insulating and thus we expect its C_a to be low and dominated by the space charge capacitance effects known for commonly investigated bulk semiconductors such as silicon and germanium. In order to identify the theoretical limits of MoS$_2$-based supercapacitors and to provide insight into charging mechanisms in this technologically important material, it is of paramount importance to study these intrinsic material properties.

In this study, for the first time, we attempt to probe C_a of chemically exfoliated, single layer MoS$_2$ in both the 2H and 1T phases. To do so, we employ a modified Langmuir-Blodgett technique[17] to functionalize atomically flat HOPG surfaces with MoS$_2$ monolayers in order to probe their differential capacitance behavior by impedance spectroscopy as a function of frequency and DC voltage. The resulting films were characterized in a spring loaded electrochemical cell to determine surface coverage, surface roughness, layer number and chemistry/phase. Using layer-by-layer deposition, single, double, and triple layer MoS$_2$ and rGO electrodes are also investigated to probe restacking effects. The results are used to estimate the theoretical limits for gravimetric and volumetric capacitance and recommendations will be made on how to increase this limit. Potential methods to enhance the intrinsic capacitance through defect engineering are also detailed.

2.5 Outline of Thesis

The main goals of this thesis work are threefold: to investigate how charge is stored in MoS_2, the limits of that storage in pure MoS_2, and how that limit can be expanded through defect engineering. Each of these three goals would greatly benefit the development of MoS_2 supercapacitor devices. To achieve these goals, we electrochemically analyze monolayer MoS_2 films deposited on flat, non-porous substrates. At the beginning of each chapter, a brief introduction will provide additional background to supplement the experimental and results sections.

Chapter 3 details the successful synthesis of nanosheet materials and assesses the method through which these nanosheets are deposited as monolayer films. Various characterization techniques are required to determine film quality. In order to approximate the fabricated electrodes as flat and non-porous, coverage must be high, and most sheets should be single layer. Additional material characterization is needed to properly isolate the intrinsic capacitance in the following chapter.

In Chapter 4, the focus is on electrochemical properties of the electrodes. Using cyclic voltammetry and electrostatic impedance spectroscopy, the mechanisms of charge storage in MoS_2 and reduced graphene oxide are examined in both aqueous and organic electrolytes. Data analysis also allows for the determination of intrinsic capacitance for both 1T and 2H MoS_2. Investigations of single, double, and triple layer films reveals the effect of restacking on both MoS_2 and reduced graphene oxide. The results are compared with expected values obtained for theory to determine how ions are arranged during charge storage. Intrinsic capacitance values are further expanded

upon to estimate potential capacitance limits for MoS$_2$ supercapacitor devices, revealing that we may have already reached the limit of pure MoS$_2$ devices.

Chapter 5 details various defect engineering strategies which allow for the enhancement of MoS$_2$ capacitance. Two primary methods are investigated: introducing sulfur vacancies and introducing edge defects. Sulfur vacancies are induced by increasing the amount of lithium intercalant used to exfoliate bulk MoS$_2$ into nanosheets. Conversely, edge defects are increased by decreasing lateral flake size through probe sonication. The results show that doubling and tripling the amount of intercalant used readily increases capacitance. However, the size-dependent capacitive behaviour of nanosheets is more complex. While decreasing flake size by 15% increases capacitance, upon size reduction by 30%, the capacitance decreases, suggesting that it is a much more limited method of defect engineering. Regardless, given careful tuning, defect engineering is shown to be a powerful tool for the enhancement of intrinsic capacitance.

Chapter 3: Langmuir Films of Molybdenum Disulfide and Reduced Graphene Oxide

3.1 Introduction

As discussed in Chapter 2, previous work on intrinsic capacitance has been focused on graphene and reduced graphene oxide, including a study by Dr. Pope in 2011[38] which measured the capacitance of functionalized graphene sheets deposited as monolayer Langmuir films. In the following chapter, I explore the possibility of applying this method to another nanosheet material, commonly used in supercapacitors: MoS_2.

The films are deposited through a horizontal precipitation method, in which droplets of a nanosheet suspension are added to a water filled trough. These nanosheets eventually densify into a monolayer film, which is then lowered onto substrates underneath through the removal of water. MoS_2 nanosheet suspensions are formed through intercalation of bulk MoS_2 powder with n-butyllithium, then exfoliation in water. Meanwhile, reduced graphene oxide (rGO) nanosheet suspensions are formed through exfoliation of bulk graphite into graphene oxide nanosheets using a modified Hummer's method, followed by reduction with hydrazine.

The nanosheet suspensions are characterized to quantify properties required to isolate the intrinsic capacitance. Once deposited as Langmuir films, the monolayers are characterized to assess film quality. High coverage films with low roughness are required in order to approximate the electrodes as flat and non-porous. Adapted with permission from Chen, J.; Walker, W. R.; Xu, L.; Krysiak, O.; She, Z.; Pope, M. Intrinsic Capacitance of Molybdenum Disulfide. *ACS Nano* **2020**. Copyright 2020 American Chemical Society.[57]

3.2 Experimental

3.2.1 Synthesis and Reduction of Graphite Oxide

Graphite oxide (GO) was synthesized using the modified Hummer's method[58] presented by Marcano *et al.*[59] 3 g of graphite (Alfa Aesar, 99.9%), 360 mL of H_2SO_4 (Sigma Aldrich, 95-98%), and 40 mL of H_3PO_4 (Sigma Aldrich, extra pure, 85% solution in water) were combined. 18 g of $KMnO_4$ (Sigma Aldrich) was added as the temperature of the water bath was raised to 40°C. The mixture was set to stir for 20 hours. After cooling to room temperature, 3 mL of 30% H_2O_2 (Sigma Aldrich) was added to the mixture dropwise, after which the colour changed from a dark brown to a light yellow. The obtained solid was transferred into a centrifuge tube in order to separate the residual acids and salts from the GO. Centrifugation was carried out at 4000 rpm for 1 hour using a Thermo Scientific Central CL2 centrifuge and suspended in water. This process was repeated once by resuspending the pellet in 30% HCl (Sigma Aldrich), followed by three cycles with ethanol (Fisher Scientific). In the end, the resulting GO suspension was stored in ethanol.

The GO nanosheets were reduced chemically with hydrazine (Sigma Aldrich, 35 wt% in water) using a modified version of Park's method.[60] A 5 mg/mL as-prepared GO suspension in ethanol was bath-sonicated for 5 minutes. Then, 2 mL of the GO suspension was diluted with 18 mL of dimethylformamide (DMF) (Sigma Aldrich, ≥99.8%), which has been shown to produce the most stable rGO nanosheet dispersions, in a 20 mL scintillation vial.[60] After the reaction chamber was heated to 140 °C and while being stirred at at 500 rpm, 80 μL of hydrazine solution was added to the reaction chamber. The mixture was set to stir for 16 hours. After the reaction

was complete, the dispersion was used immediately as obtained for film deposition to minimize the chance of agglomeration.

3.2.2 Exfoliation of Molybdenum Disulfide

Bulk molybdenum disulfide was exfoliated chemically with n-butyllithium using a modified version of Eda's method.[17] 0.5 g of MoS_2 powder (Sigma Aldrich, ~6 µm) was mixed with 7 mL of 1.6 M n-butyllithium solution in hexane (Sigma Aldrich) in a 25 mL reaction vessel. After stirring continuously for three days in an Ar-filled glove box (O_2 and H_2O < 1ppm), the intercalated MoS_2 was collected by filtration into a large beaker, washed with 80 mL of hexane, and diluted with 150 mL of deionized water. Then, the beaker was bath sonicated (TruSonik, 2.5 L, 120 W) for 1 h to complete the exfoliation process. Following sonication, the dispersion was subjected to a solvent exchange method to transfer it to DMF.[17] HCl solution was used to adjust the pH of the dispersion to 2, flocculating the MoS_2. The aggregates of MoS_2 were collected by filtration using Whatman 42 filter paper, then transferred into a centrifuge tube and redispersed in DMF by bath sonication.

3.2.3 Characterization

The C/O ratio of the reduced GO (rGO) nanosheets was estimated by energy-dispersive X-ray spectroscopy (EDS) on powders formed by drying dispersions in a vacuum oven at 110 °C and found to be ~5.2. A study was carried out to maximize the reduction of GO without causing agglomeration of the dispersion, by varying the reaction temperature and hydrazine addition.

X-ray photoelectron spectroscopy (XPS) was performed on MoS_2 samples with a Thermo-VG Scientific ESCALab 250 X-ray Photoelectron Spectrometer Microprobe, using a

monochromatic Al Kα X-ray source (1486.6 eV). Samples were prepared by drop casting aqueous

MoS_2 nanosheet suspensions onto Si wafers, followed by drying in a vacuum oven without heat.

CasaXPS was used to deconvolute the core-level spectra. The relative contribution of the 1T and

2H phase to the Mo^{4+} $3d_{3/2}$ and Mo^{4+} $3d_{5/2}$ was used to calculate the 2H content, as described by

Papageorgopoulos et al.[19,61] Meanwhile, a SpectraMax M2 Microplate Reader with a cuvette port

was used for UV-Vis spectroscopy to estimate the 1T/2H ratio of the MoS_2 nanosheets. The 2H

content of MoS_2 can be estimated using an empirical relation derived by Knirsch et al.[62] E_{410} and

E_{350}, which represent the absorbance at 410 nm and 350 nm, respectively, were used in the

following equation to calculate 2H ratio:
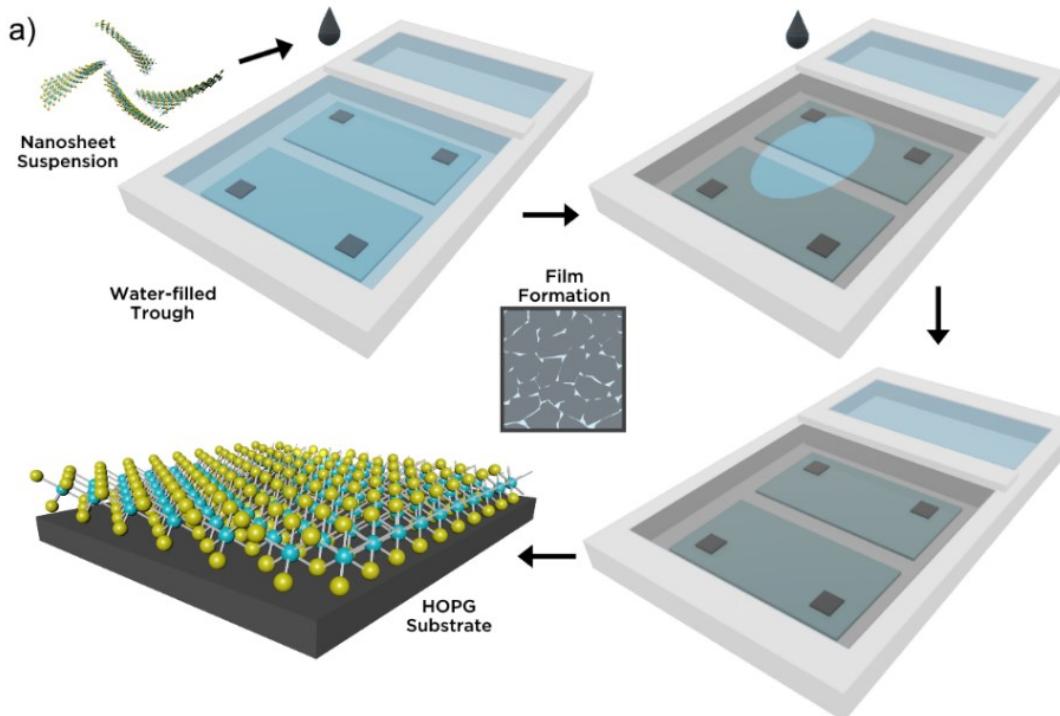
$$\frac{2H}{1T+2H} = 1.29 - 2.562 \times 0.287^{\frac{E_{410}}{E_{350}}} \quad (2)$$

The absorbance obtained at 350 nm is associated with strong 1T contribution while the absorbance

at 410 nm is related to strong 2H contribution.[62]

3.2.4 Preparation of Monolayer Electrodes

Prior to preparation of the deposited dispersion, the nanosheet suspensions in DMF were

sonicated for 10 minutes. Then, the nanosheet suspensions were diluted with equal parts DMF

and 1,2-dichloroethane (DCE) until concentrations of 0.055 mg/mL and 0.00625 mg/mL were

achieved for the MoS_2 and rGO nanosheet suspensions, respectively. Fairly dilute nanosheet

dispersions and a water immiscible, volatile spreading solvent such as DCE are required for

successful deposition.[17] Aggregates were removed by centrifugation in 15 mL glass tubes at

3500 rpm for 1 hour prior to deposition using an Fisher Scientific AccuSpin 3 centrifuge.

Monolayer films were deposited onto the air-water interface of a polytetrafluorethylene (PTFE) trough, as shown in Figure 8. The total available water surface area (15.8 cm x 12.7 cm) for film formation was approximately 200 cm^2. The trough was first cleaned by rinsing with deionized water and wiped with DCE. Dispersions were then added to the air-water surface *via* a syringe pump (KD Scientific) using a glass syringe equipped with PTFE tubing (0.312 mm outer diameter) at a flow rate of 0.13 mL/min. The end of the tubing was positioned such that the droplet formed was just above the air-water interface. Too high of a position can lead to penetration of the drop through the air-water interface and into the bulk instead of spreading on the surface as is required for successful transfer. Deposition was carried out until approximately 20% of the ~200 cm^2 water surface remained uncovered by the film of densely tiled nanosheets. Then, the film was compressed until the entire surface was covered.

Figure 8. Illustration of modified Langmuir-Blodgett deposition method

The horizontal precipitation method[16,17,38,42] was used to deposit the floating films of rGO or MoS$_2$ onto various clean substrates placed under the water prior to deposition. These included freshly cleaved mica and HOPG, as well as clean glass slides and SiO$_2$ wafers. Double and triple layer films were fabricated by repeated deposition on already coated substrates after drying the substrates for 1 min on a hot plate at 60 °C. To restore the 2H phase of the MoS$_2$ films, 1T MoS$_2$ electrodes were heat-treated at 300 °C, according to a process reported by Acerce *et al.*[18] Electrodes were placed in a quartz tube which was purged and filled with Ar (99.999%) three times. Then, the electrodes were annealed at 300 °C in a furnace (Lindburg Blue M) under argon with a 10 sccm flow for 1 hour. Additional samples were annealed at 150 °C to obtain an intermediate 2H content.

3.2.5 Characterization of Monolayer Films
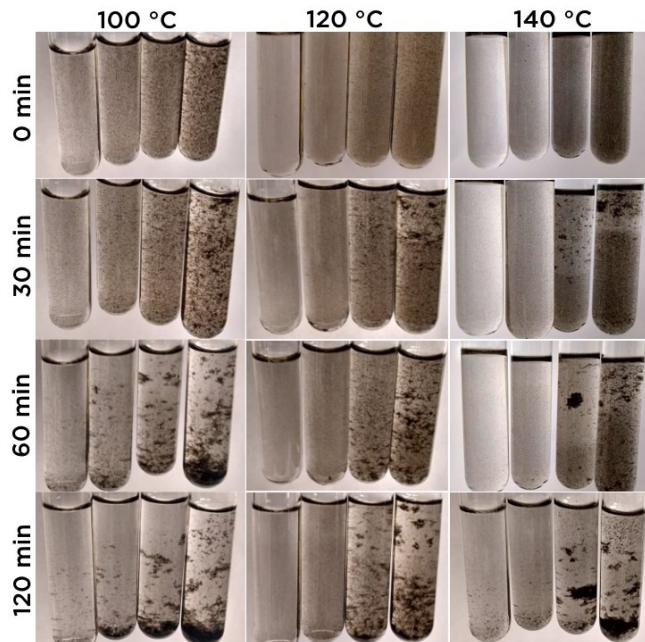
Single, double, and triple layer rGO and MoS$_2$ films were characterized using UV-Vis spectroscopy to determine the transmittance on glass substrates. Atomic force microscope (AFM) images were taken using a Digital Instruments Nanoscope IV to determine flake size, roughness, and film coverage using contact mode and Bruker, NP-STT10 tips. These images were assessed using Gwyddion software to determine surface roughness, by dividing the projected area of the sample by the measured surface area. Python code was also used to determine fractional coverage and average sheet thickness. This script fit the raw height data of the image to a sum of Gaussian curves representing sheets of various average thickness. The area under these curves and height corresponding to their peak centers were taken as the fractional coverage and average film thickness, respectively. Film coverage was also observed by scanning electron microscopy (SEM)

using a field emission scanning electron microscope (LEO 1550, Zeiss) with an acceleration voltage of 10 kV. These SEM images were analyzed using ImageJ.
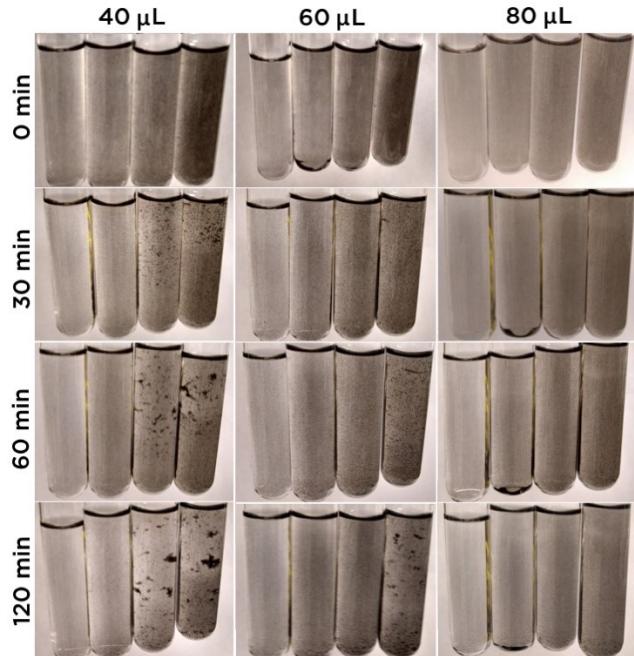
3.3 Results

3.3.1 Characterization of Exfoliated Materials

The parameter study demonstrated that rGO dispersions formed at higher temperatures and with greater hydrazine content showed greater stability, as shown in Figures 9 and 10. In every image, the rGO nanosheet concentrations in the vials are 0.00625, 0.0125, 0.01875, 0.025 g/L from left to right, while the reaction temperature or hydrazine content is indicated by the column header. rGO nanosheets that were more completely reduced and therefore more hydrophobic allowed for better dispersion in 1:1 DMF:DCE. This reduced aggregation in the nanosheet solutions and produced higher quality Langmuir films.
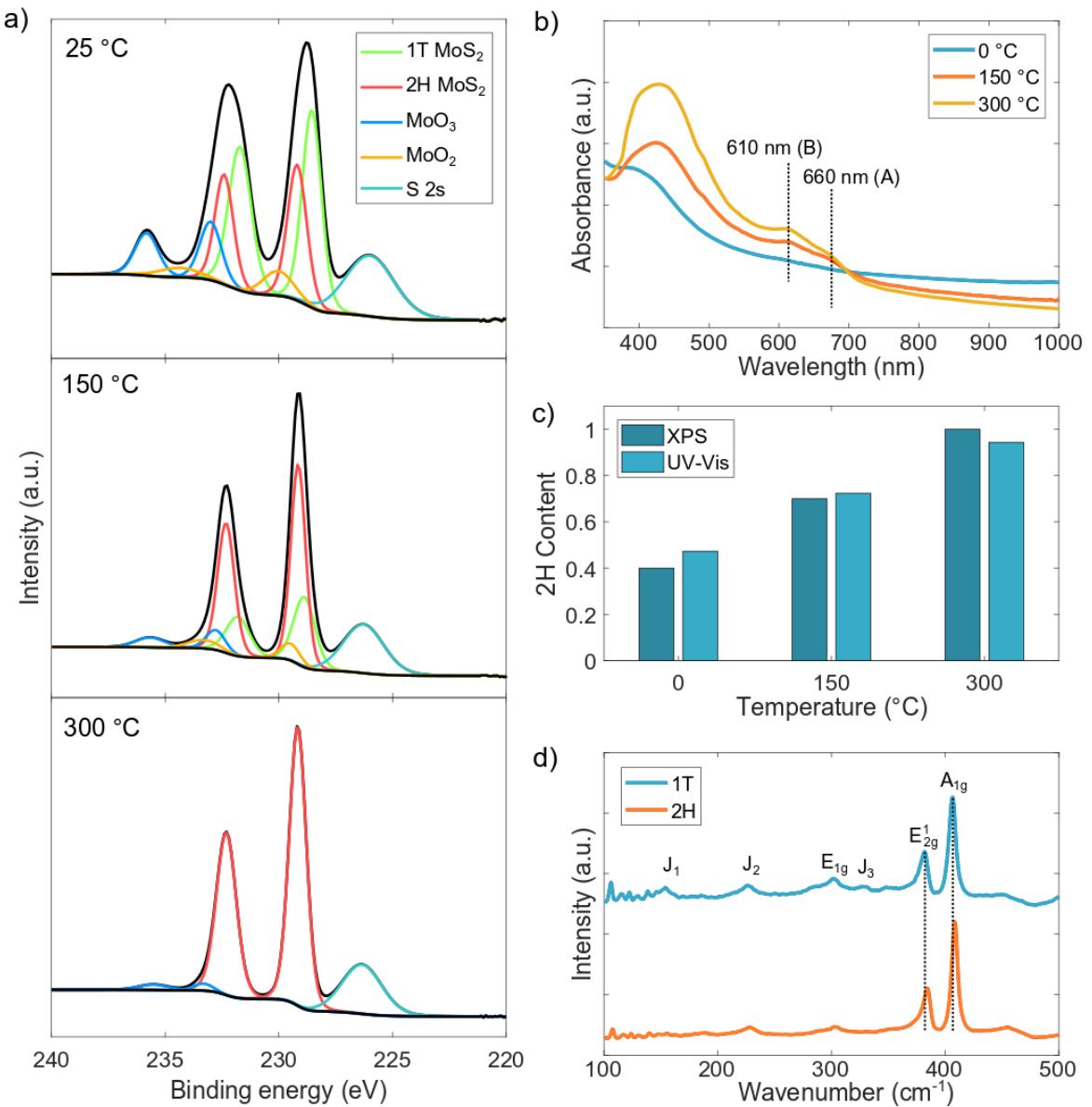
Figure 9. Reduction of graphene oxide with 20 µL of hydrazine in various temperatures. In every image, the rGO nanosheet concentrations in each vial are 0.00625, 0.0125, 0.01875, 0.025 g/L from left to right

Figure 10. Reduction of graphene oxide with various amounts of hydrazine at 140 degrees Celsius. In every image, the nanosheet concentrations in each vial are 0.00625, 0.0125, 0.01875, 0.025 g/L from left to right.

Figure 11a shows the XPS spectra of the Mo 3d state for samples before and after heat treatment at 150 °C and 300 °C, as well as deconvolution of the spectra obtained by curve fitting. Papagerogopoulas and Jaergerman reported the sensitivity of XPS to the differences in the Fermi levels in 1T and 2H MoS_2.[61] Following heat treatment, the contribution of 1T MoS_2 (green) to the binding energy of Mo^{4+} $3d_{5/2}$ and Mo^{4+} $3d_{3/2}$ is almost entirely diminished, shifting peak positions lower by ~0.7 eV with restoration of the 2H MoS_2 phase (red). By calculating the area under the 1T and 2H MoS_2 peaks, we can obtain the phase composition for each sample. For untreated samples, the 2H content was 39.8%, while the 2H content of samples treated at 150 °C was 70.7% and the 2H content of samples treated at 300 °C was 100%. This is in good agreement with results previously reported by Eda *et al.*[21]

Figure 11. a) XPS spectra (black) of MoS_2 following heat treatment at various temperatures and corresponding fitted curves for 1T MoS_2, 2H MoS_2, S 2s, MoO_3, and MoO_2, b) UV-Vis absorption spectra of MoS_2 dispersion, c) comparison of 2H content calculated from XPS and UV-Vis data, and d) Raman spectra of the MoS_2 before (blue) and after (orange) heat treatment at 300 °C
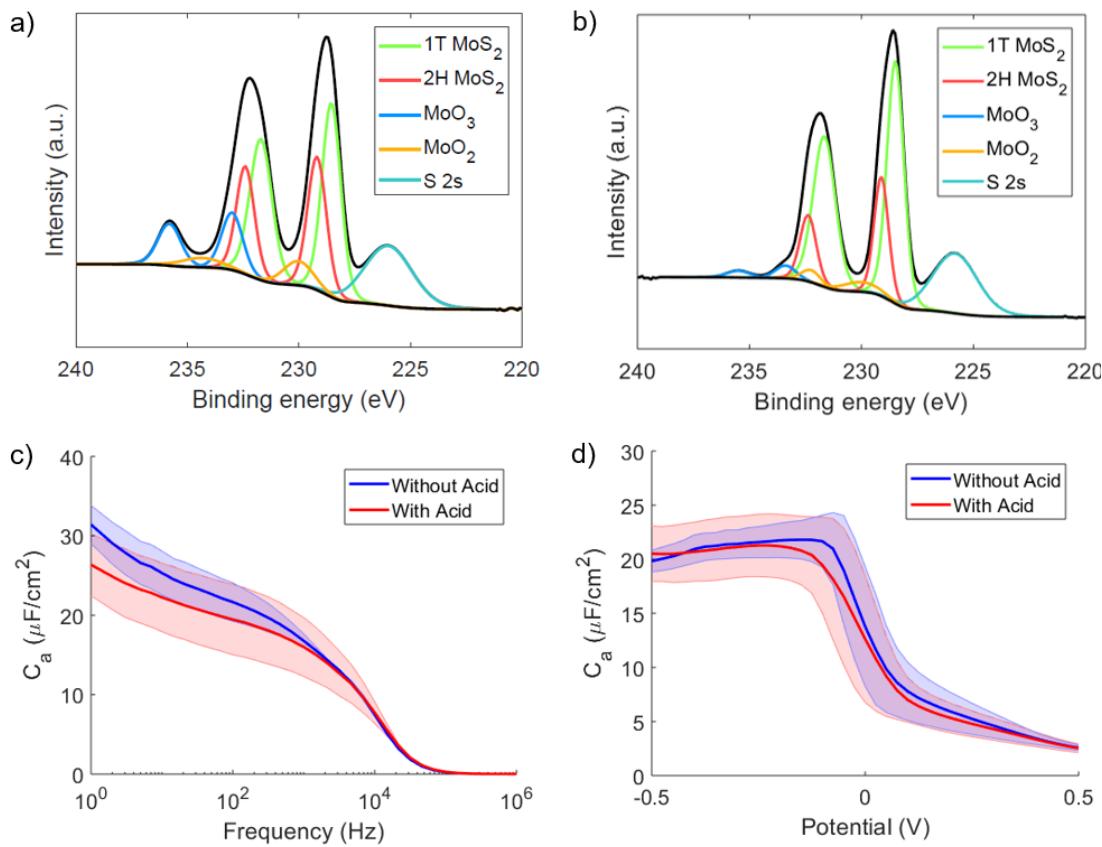
A complete breakdown of the sample composition as determined by XPS can be found in Table 1. The XPS results also indicate the presence of MoO_2 and MoO_3 which comprise 5.72% of the bulk MoS_2 powder but are also formed during processing when the material is exposed to light and oxygen *via* a recently reported mechanism.[63] The untreated samples showed 22.4% MoO_x content, which was reduced to 17.1% MoO_x content following heat treatment at 150 °C, and further reduced to 3.61% MoO_x content at 300 °C.

Table 1. Percentage of the individual component estimated by the integrated areas of the fitted Mo3d core level spectra.

Sample	1T MoS_2	2H MoS_2	MoO_3	MoO_2	2H/(1T+2H)	MoO_x
Untreated	46.73	30.84	14.85	7.57	39.76	22.42
Partially Treated	24.92	60.21	7.88	7.00	70.73	14.87
Treated	0	96.39	3.61	0	100.00	3.61

Figure 12 shows the effect of acid flocculation on the measured capacitance of MoS_2. Figures 12a and 12b compare the XPS spectra of MoS_2 nanosheets fabricated with and without acid flocculation, respectively. Solvent exchange of MoS_2 nanosheets from water to DMF is performed through filtration of the aqueous suspension, and if nanosheets are not flocculated, the process can take several hours at a time. Acid flocculation is typically employed to expediate the solvent exchange process, reducing the time needed from several hours to a few minutes. From the spectra, it is clear that acid flocculation results in the increased presence of MoO_x compounds and analysis of the results indicate an increase from 12% to 22% composition if acid flocculation is used. This can potentially be explained by the formation of superoxide in MoS_2 upon exposure to light, which reacts with water and MoS_2 to form MoO_3.[63]

Previous reports of MoS_2 nanosheets synthesized through intercalation of bulk MoS_2 with n-butyllithium have shown XPS spectra with similar or even higher levels of MoO_x.[63–67] When the relative percentage of Mo^{6+} 3d peak, associated with MoO_x, is presented, it is between 10.0% to 11.4%, which is comparable to that of our unfloccuated samples.[63,66,67] Figures 12c and 12d show areal capacitance as a function of frequency and potential obtained from electrochemical impedance spectroscopy (EIS) measurements for MoS_2 nanosheets synthesized with and without acid flocculation, respectively. From the EIS results, it is clear that any deviation between samples falls well within the standard deviation of the measurements.

Figure 12. XPS data of MoS_2 nanosheets fabricated a) with and b) without acid flocculation. Areal capacitance measured as a function of c) frequency at -0.1 V and d) potential at 100 Hz for monolayer films deposited from MoS_2 fabricated with and without acid flocculation

The phase composition results were validated by UV-Vis measurements of the MoS_2 dispersion, shown in Figure 11b, which are in agreement with previously reported results.[17] The peak observed between 350-450 nm indicates a direct excitonic transition from the valence to the conduction band, and is enhanced upon transforming 1T MoS_2 to the 2H polymorph through heat treatment.[68] Similarly, the peaks observed at ~610 nm and ~660 nm correspond to B1 and A1 direct excitonic transitions in 2H MoS_2, respectively. The peaks at ~610 and ~660 nm are only observed in the 2H MoS_2 sample.
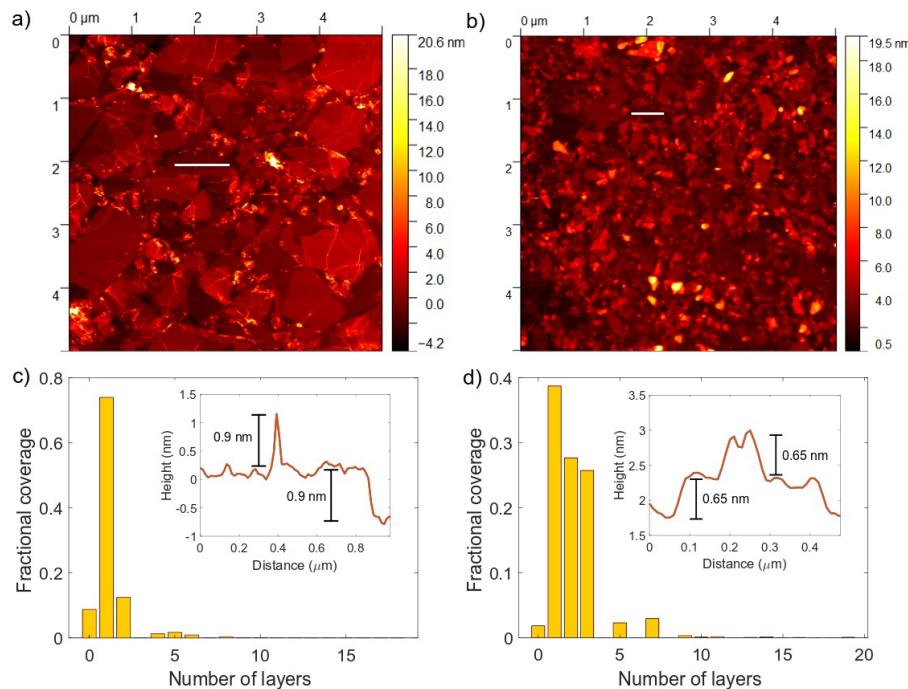
As shown in Figure 11c, or untreated samples, the 2H content is estimated from the UV-Vis data using the empirical relation suggested by Knirsch *et al.*[69] as 47.3% while the 2H content of samples treated at 150 °C is 72.3% and the 2H content of samples treated at 300 °C is 94.4%. This estimate is in good agreement with the XPS results and further validates the accuracy of this relationship using much easier to obtain UV-Vis data. For brevity, in the rest of the thesis we refer to the untreated samples and samples treated at 300 °C as '1T MoS_2' and '2H MoS_2', respectively; However, they are more accurately '1T-rich' and '2H-rich' samples.

Raman spectroscopy results are shown in Figure 11d and used to confirm 1T to 2H phase transition following heat treatment. Peaks can be observed at ~382 cm^{-1} (E^1_{2g}) and ~407 cm^{-1} (A^1_g) for both samples, which are vibrational modes respectively associated with in-plane and out-of-plane vibrations of 2H MoS_2.[17] The broadening and shifting of these peaks to lower wave numbers after exfoliation are typical of the 1T phase.[2] In the 1T MoS_2 sample, three characteristic peaks are observed at 154 cm^{-1}, 226.1 cm^{-1}, and 326.4 cm^{-1}, also known as the J_1, J_2, and J_3 peaks. These

peaks, indicative of 1T MoS$_2$, are significantly diminished following heat treatment, suggesting

transformation into the 2H phase.[17]

3.3.2 Characterization of Monolayer Langmuir Films and Coated Substrates
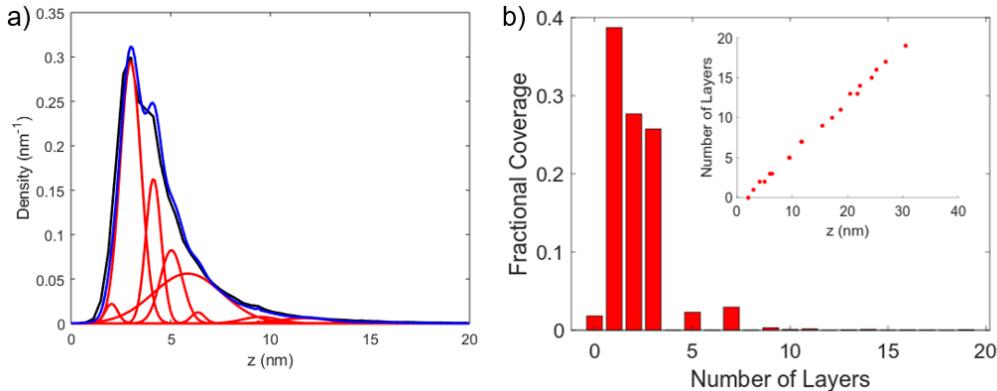
Figures 13a and 13b illustrate typical AFM images of the Langmuir films coated onto

HOPG. The films are composed of densely tiled flakes. In the case of rGO (Fig. 13a), the thickness

of a monolayer is approximately 0.7-1.0 nm, as determined by Gwyddion height profiles, which

is in good agreement with the typical thickness observed for single layer rGO.[16] Likewise, double

layer nanosheet was found to be 1.8 nm thick. The surface roughness was calculated to be 1.01 ±

0.002 and did not vary significantly between layer number or material. rGO films showed

wrinkled flakes with diameters on the order of microns, as seen in Figure 13a.

Figure 13. AFM images of a) rGO and b) MoS$_2$ films on HOPG substrates and height distribution of these c) rGO and d) MoS$_2$ films. Height profiles from the AFM images are shown in the inset of the height distribution plots.

As mentioned in the Experimental Methods section, a Python script was used to fit a sum of Gaussians to the raw height data, resulting in a calculation for fractional coverage by layer number. An illustration of how the script fits Gaussian functions to the height distribution can be seen in Figure 14. A comparison between the sum of Gaussian line shapes to the raw height data is shown in Figure 14a, where the black line shows the raw height data, the red lines show the individual Gaussian functions, and the blue line shows the sum of each Gaussian function. Measured monolayer thickness was input as the first guess for layer thickness.

Figure 14b shows the corresponding histogram of fractional coverage by layer number for an MoS_2 monolayer sample. The slope of the curve is 1.5 nm/layer, which reveals the thickness of a single layer. This is in good agreement with previously reported thickness values for chemically exfoliated MoS_2 monolayers.[70] Deviation from the expected thickness of 0.65 nm/layer can be explained by surface defects or leftover solvent trapped between monolayers.[17]
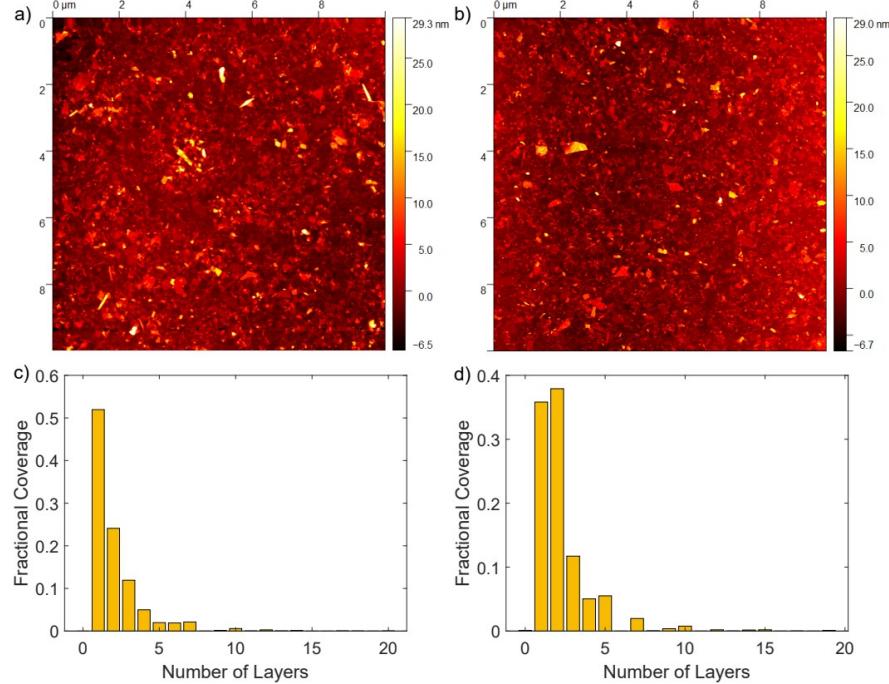
Figure 14. a) Height distribution plotted against Gaussian fit and b) fractional coverage by layer number

In the rGO sample, 92.2% surface coverage is obtained, with 74.0% of the surface covered by monolayers and 18.2% covered by two or more layers. The MoS_2 films displays a less wrinkled morphology, and the sheet sizes are often smaller than 1 μm in diameter, as shown in Figure 13b. For MoS_2, the thickness of a monolayer is approximately 0.65 nm, which is demonstrated by the thickness profile of a single nanosheet.[71] Similarly, a double layer is found to be 1.3 nm thick. In this sample, 97.7% surface coverage is obtained, with 38.7% coverage by monolayers, 27.7% coverage by bilayers, and 31.3% coverage by three or more layers.

Despite a generally uniform coating, the MoS_2 films are occasionally interspersed with chunks of material up to 25 nm thick. These aggregates are likely caused by incomplete intercalation of bulk MoS_2 since they are orders of magnitude larger than 0.65 nm, the expected thickness of single layer MoS_2.[71] Since lithium is unable to intercalate these chunks, it is reasonable to assume that the electrolytes used are unable to do so, as well. Therefore, the presence of the chunks should not contribute considerably to the areal capacitance of the electrode. This assumption will be further validated in the electrochemical results discussion below.
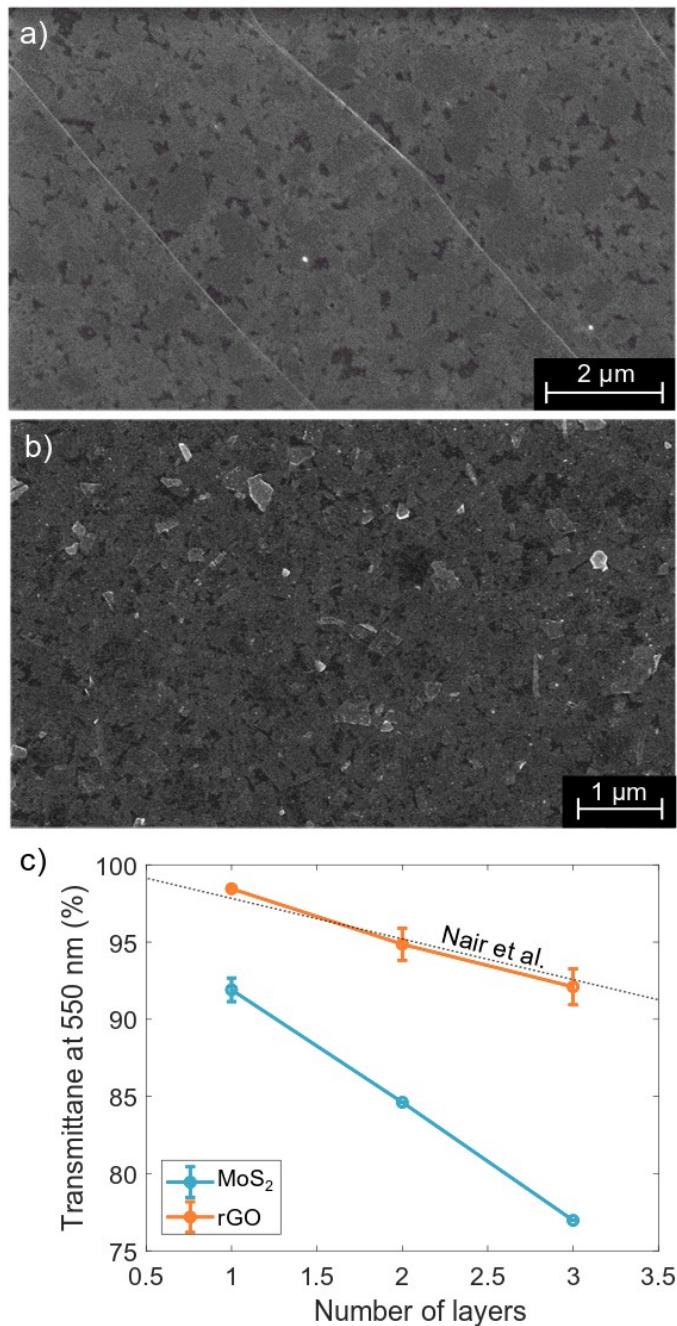
To compare the effect of different centrifugation speeds on monolayer MoS_2 film formation, films were deposited from nanosheet suspensions centrifuged at 3500 rpm and 4150 rpm, as shown in Figures 15a and 15b, respectively. A qualitative comparison of Figures 15a and 15b shows that the 25 nm thick chunks are present despite centrifugation. Quantitative comparison using Gwyddion analysis produced height distributions for both samples, as shown in Figures 15c and 15d.
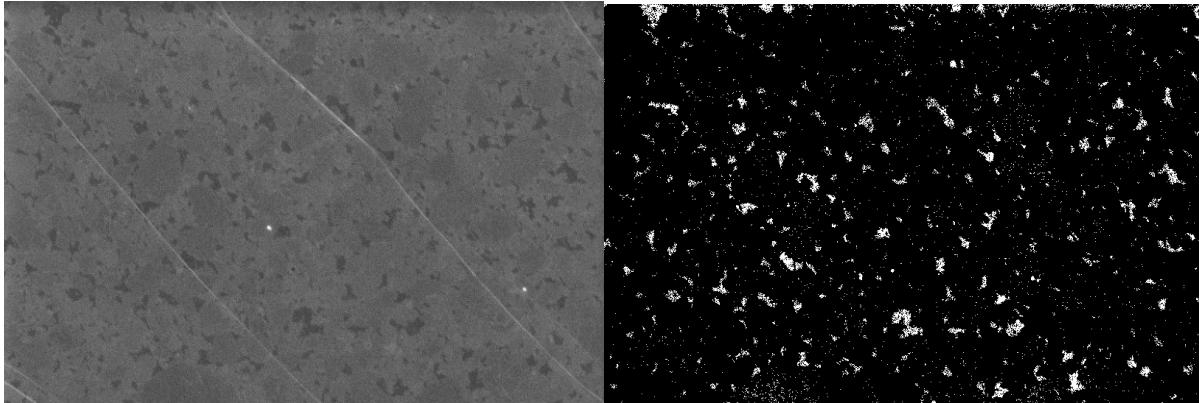
Figure 15. AFM images of MoS$_2$ films deposited from nanosheet suspensions centrifuged at a) 3500 rpm and b) 4150 rpm, as well as height distribution of films deposited from suspensions centrifuged at c) 3500 rpm and d) 4150 rpm

This analysis reveals that there is little difference between the calculated coverage, found to be on average 2.09 ± 0.03 and 2.01 ± 0.26 layers for films deposited from suspensions centrifuged at 3500 rpm and 4150 rpm, respectively.

SEM images shown in Figure 16 demonstrate the film coverage over larger areas. ImageJ was employed to determine the fractional coverage of the films through pixel counting, as detailed in Figure 17. First, an image is selected. Then, the image is converted into a binary of either white or black pixels by applying the default threshold. Black pixels represent the presence of a sample on the substrate white pixels indicate bare substrate. Each type of pixel is counted, and the percentage of black pixels is considered fractional coverage.

Figure 16. SEM images of a) rGO and b) MoS₂ films on HOPG substrates and c) transmittance at 550 nm of MoS₂ and rGO films as a function of coating layers

Figure 17. SEM images before (left) and after (right) conversion to binary
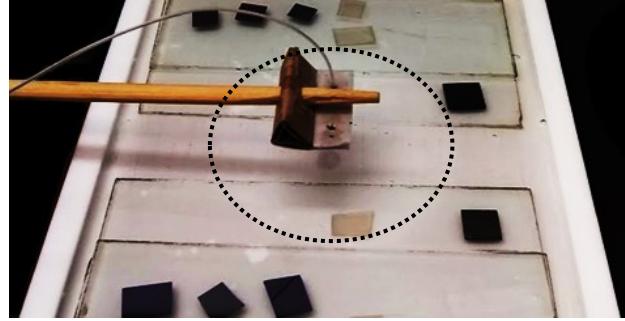
rGO films possess an average fractional coverage of 87.9 ± 3.5%. Conversely, MoS_2 films exhibited an average coverage of 92.1 ± 1.6%, which is in agreement with the values obtained from AFM image analysis. This is evident in Figure 16, which shows denser tiling for the rGO film compared to the MoS_2 film. As the number of layers increases, MoS_2 film coverage jumps to 100% for double and triple layer films as the underlying substrate could no longer be identified.

3.3.3 Characterization of Multilayer Langmuir Films and Coated Substrates

Since it was not possible to probe the thickness of bi and trilayer films accurately by AFM due to the lack of exposed substrate, we relied on UV-Vis to confirm the thickness scaled linearly with layer number. Glass substrates were coated with monolayer, bilayer, and trilayer Langmuir films of both materials, and their transmittance was measured. As shown in Figure 16c, a monolayer rGO film exhibits a transmittance of 97.6% at 550 nm, when corrected with film coverage, decreasing by 2.1-2.8% with every further deposition.

This is in good agreement with the theory and results presented by Nair *et al*, which showed that a graphene monolayer absorbs 2.3% of white light.[72] Conversely, a 1-layer MoS_2 film exhibited a transmittance of 92%, decreasing by 7-8% with every further deposition. This is

comparable to previously reported values, which claimed 90% transmittance for single layer MoS_2, decreasing by 8-10% per added layer.[17] An image of a complete modified Langmuir film can be found in Figure 18. The formed film is densely tiled and appears continuous, save for the empty patch in the middle.

Figure 18. Photo of modified Langmuir film formation

3.3.4 Transfer Efficiency of Langmuir Films

The transfer efficiency can be calculated using the Langmuir specific surface area (LSSA) calculated using the following formula: $LSSA\left(\frac{m^2}{g}\right) = \frac{A_{film}}{v \times t \times C}$, where A_{film} is the total area of film on the water surface, v is the deposition rate (in mL/min) controlled by the syringe pump, t is the total deposition time and C is the MoS_2 concentration.

For MoS_2, the value is: $LSSA\left(\frac{m^2}{g}\right) = \frac{2 \times 0.8 \times (200\ cm^2)}{(0.13\frac{mL}{min}) \times (20\ min) \times (0.055\frac{mg}{mL})} = 240\frac{m^2}{g}$

For rGO, the value is: $LSSA\left(\frac{m^2}{g}\right) = \frac{2 \times 0.8 \times (200\ cm^2)}{(0.13\frac{mL}{min}) \times (25\ min) \times (0.00625\frac{mg}{mL})} = 1576\frac{m^2}{g}$

However, for the rGO we used the mass of GO in this expression as this was known experimentally prior to reduction. It is expected that the mass of rGO would be less due to the loss of oxygen-containing functional groups from the material. Due to the low concentration we could not effectively measure the concentration of rGO and thus the calculated value provides an

underestimate of the LSSA. We can compare these values to the theoretical surface area of graphene and MoS_2 which are 2630 m^2/g and 636 m^2/g, respectively. By dividing the LSSA by the SSA, we can estimate an average layer thickness assuming the film is dense. This calculation estimates that the MoS_2 film is 2.65 layers thick on average and that the rGO film is 1.67 layers thick on average. This is comparable, though higher, than the average thicknesses calculated through AFM analysis, which are 2.13 layers for MoS_2 and 1.23 layers for rGO.

3.4 Conclusion

In this chapter, the synthesis of MoS_2 and rGO nanosheets is shown to be successful, resulting in well exfoliated materials in both cases. The optimum procedure for reduction of GO by hydrazine was found by changing relevant parameters, such as hydrazine content and reduction temperature. The parameter study produced stable colloidal dispersions of rGO in DMF and DCE, which were easily deposited as monolayer films.

The deposited films for both samples were of high quality, demonstrating low roughness and coverage of above 85% for all samples. These results suggest that it would be reasonable to approximate the monolayer electrodes as flat and non-porous, therefore, they could be used for measurement of the intrinsic capacitance. Multilayer films appear to be of similar quality. Furthermore, extensive material characterization through UV-Vis and XPS allowed for phase composition analysis of the MoS_2 nanosheet dispersion, as well as determination of other material properties required to isolate the intrinsic capacitance. The results show complete conversion to the 2H MoS_2 phase following heat treatment at 300 °C.

Chapter 4: Intrinsic Capacitance and Charge Storage Mechanisms of MoS$_2$ Nanosheets

4.1 Introduction
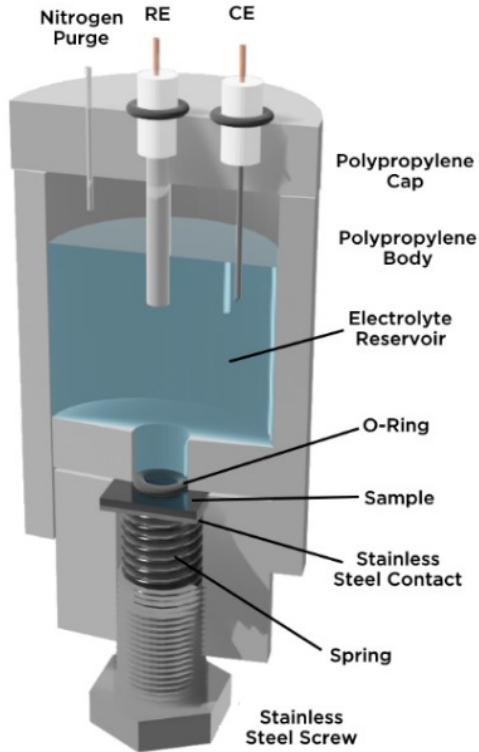
In the following chapter, the electrochemical properties of the monolayer and multilayer electrodes are investigated through cyclic voltammetry and intrinsic capacitance. Measurements are carried out in both aqueous and organic electrolytes, and the measured capacitance is analyzed over a frequency range of 1 to 10^6 Hz and a potential range of -0.3 to 0.5 V. The results of these measurements are used to gain insights on how MoS$_2$ and rGO are affected by restacking effects. Furthermore, the charge storage mechanisms of 1T and 2H MoS$_2$ are explored.

From this data, the intrinsic capacitances of 1T and 2H MoS$_2$ are calculated and compared to expected values from theory. Through dimensional analysis of the results, estimated values for capacitance limits of MoS$_2$ supercapacitors are made. Adapted with permission from Chen, J.; Walker, W. R.; Xu, L.; Krysiak, O.; She, Z.; Pope, M. Intrinsic Capacitance of Molybdenum Disulfide. *ACS Nano* **2020**. Copyright 2020 American Chemical Society.[57]

4.2 Methods

4.2.1 Electrochemical Characterization of Monolayer Electrodes

The electrodes were characterized using a custom-made 3D printed polypropylene electrochemical cell mimicking the same design previously reported that used machined polytetrafluorethylene.[38,42] In this configuration, the exposed surface area of the electrodes was controlled *via* spring-loading against an O-ring, as shown in Figure 19.

Figure 19. Schematic diagram of three-electrode electrochemical cell
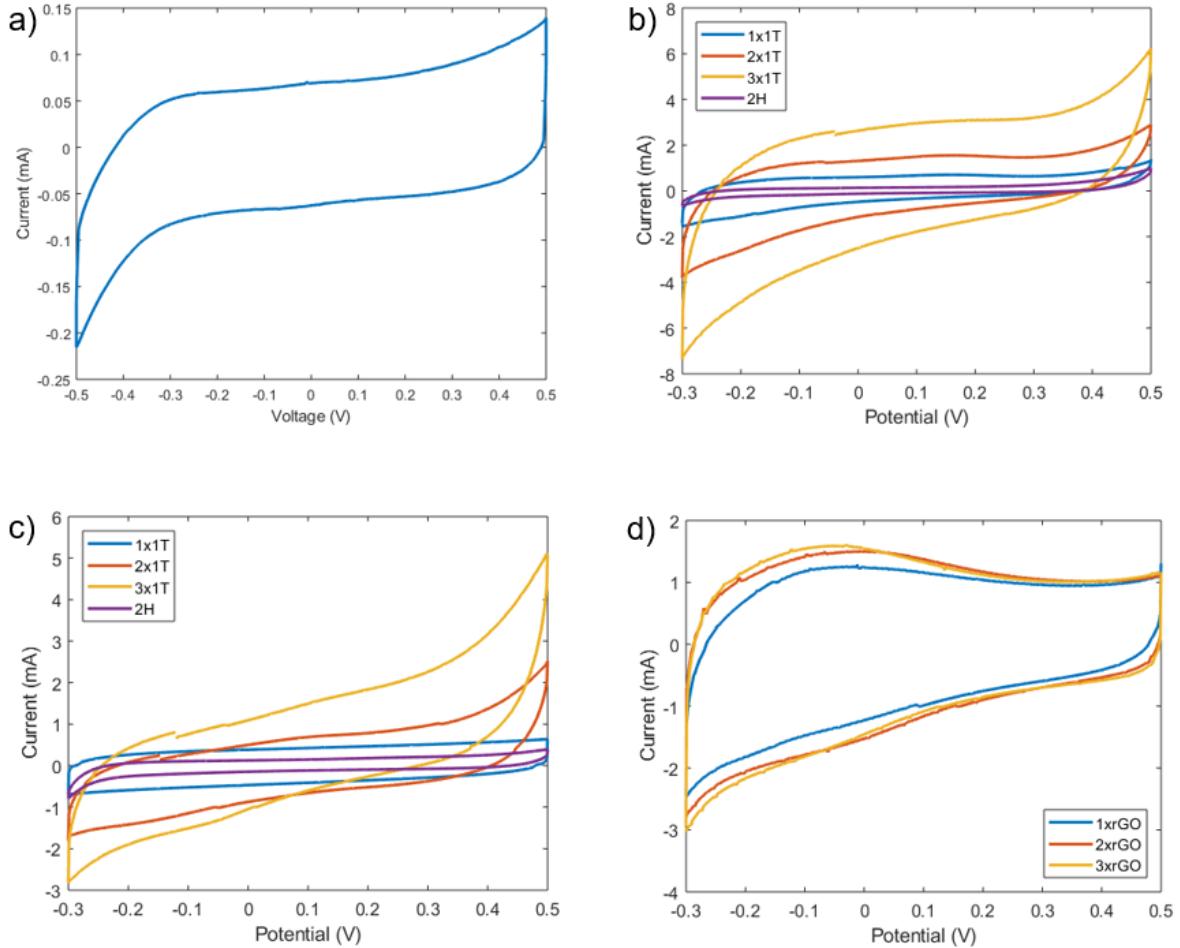
For testing in aqueous electrolyte, 1 M NaF dissolved in ultra-high purity Milli-Q water was used as the electrolyte. This was used in an attempt to eliminate specific adsorption as NaF is relatively non-adsorbing and often used in fundamental studies of double-layer charging.[39,43,44] A Ag/AgCl reference electrode (1 M) and Pt wire counter electrode (0.5 mm diameter, 99.99% purity) were used. For testing in organic electrolyte, the cell was filled with 0.1 M tetrafluoroborate (TEABF$_4$) in acetonitrile (AN) and two Pt wires were used as a quasi-reference and counter electrode. 1 mM ferrocene was added to the electrolyte immediately after the measurement to define the reference potential using cyclic voltammetry. Perfluoroelastomer O-rings were employed to minimize swelling in organic electrolytes.

Cyclic voltammetry (CV) and electrochemical impedance spectroscopy (EIS) were conducted with a SP-300 potentiostat (Bio-Logic USA). Samples were tested in a voltage window of -0.3 to 0.5 V. This voltage window was chosen because apparent faradaic reactions would occur at voltages greater than 0.5 V and less than -0.3 V. Potential dependent capacitance behaviour was typically plotted at 100 Hz in an attempt to eliminate slower Faradaic charging processes from the measurement while frequency dependence was plotted at -0.14 V vs. Ag/AgCl (1 M), the approximate open circuit potential of all coated samples.

4.3 Results

4.3.1 Electrochemical Characterization of HOPG Substrates

Cyclic voltammograms (CVs) obtained at 100 mV/s for pure HOPG are rectangular in nature from voltages of -0.5 V to 0.5 V, as seen in Figure 20, with a small enhancement of cathodic current below about -0.3 V likely generated by the reduction of residual oxygen in the cell. This oxygen reduction was found to cause a significant and irreversible increase in capacitance over the entire potential window likely caused by the reactive oxygen species generated (ex. H_2O_2). The reactive oxygen species would then interact with the MoS_2, forming either soluble molybdates and high activity edge sites, or possibly pseudocapacitive MoO_3.[63] Because of this, a voltage window of -0.3 V to 0.5 V is used to avoid damaging the films.
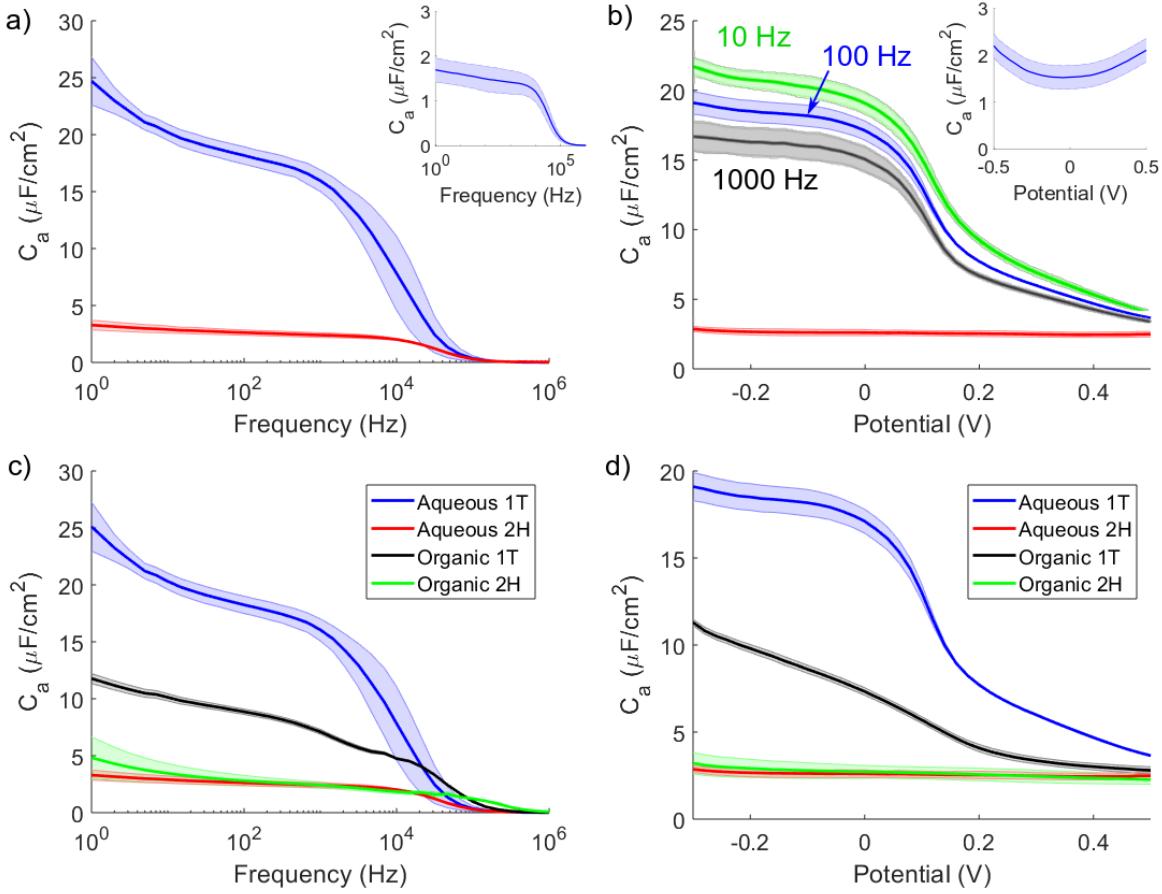
Figure 20. CV profiles obtained for a) HOPG in aqueous electrolyte, for 1T and 2H MoS2 single, double, and triple layer electrodes in b) aqueous and c) organic electrolytes, and d) for rGO single, double, and triple layer electrodes in aqueous electrolyte.

4.3.2 Characterization of Monolayer MoS$_2$ Films in Aqueous Electrolyte

As shown in Figure 21, EIS is used to investigate the capacitance of all films as a function of frequency and DC potential. The lines in the plot represent average values of three or more runs while the shaded regions represent the ± standard deviation of the measurement. The inset of Figure 21a and 21b shows that the capacitance of the bare HOPG ranges from 1.5 to 2 µF/cm^2 between -0.3 to 0.5 V. This is only slightly lower than the 2 to 3 µF/cm^2 reported in literature but the capacitance of HOPG is known to be influenced by quality of the crystal and number/density of edge-planes exposed.[38,43,44] The capacitance remains fairly constant with

frequency, showing less than 19.2% change between 10 and 1000 Hz. The voltage dependence curve in the inset of Figure 21b demonstrates a rounded V-shape with a minimum occurring close to -0.1 V vs. Ag/AgCl (1 M) which coincides with the OCP. This is similar to what has been reported by Randin and Yeager in their pioneering studies.[43,44]

Figure 21. Areal capacitance of 1T (blue) and 2H (red) MoS$_2$ films in aqueous electrolyte as a function of a) frequency at -0.14 V vs. Ag/AgCl (1 M) and b) potential at 100 Hz for 2H MoS$_2$ and at various frequencies for 1T MoS$_2$, with corresponding measurements on bare HOPG in the inset. Comparison between areal capacitance of 1T and 2H MoS$_2$ films in aqueous and organic electrolyte as a function of c) frequency at -0.14 V vs. Ag/AgCl (1 M) and d) potential at 100 Hz

For the MoS$_2$, the 1T films in particular, below about 10 Hz, the slope of the capacitance-frequency curves typically increased significantly due to slower Faradaic charging processes. Thus 100 Hz is chosen for comparing between films as this frequency is also sufficiently far away from the knee frequency dictated by the RC time constant of the cell.[73] Depending on the film capacitance and the position of the reference electrode (which we attempted to keep the same for each measurement) the knee frequency ranges from 10^4-10^5 Hz.

The most obvious difference in the frequency dependence curves is the large difference in the magnitude of the capacitance between 1T and 2H MoS$_2$. As shown in Figure 21b, this considerable difference in capacitance exists only at potentials more negative than the OCP until the capacitance of the 1T MoS$_2$ drops significantly after reaching 0.1 V, and continues to decrease past that point, while 2H MoS$_2$ shows comparatively little voltage dependence. The large difference observed under negative polarization might be expected due to the metallic vs. semiconducting nature of the two materials.[18]

However, the complex voltage dependence of the 1T MoS$_2$ material is surprising and not readily explained. For example, we might consider these changes a result of changes to the Stern layer (adsorbed ions or adsorbed solvated ions that make up the inner vs. outer Helmholtz planes) at either side of the point of zero charge (pzc), which as approximated as the OCP, or potential-dependent pseudocapacitance (*i.e.*, intercalation, redox active function groups) or possibly potential dependent electronic effects within the material itself.

42

If we first consider the Stern model, under positive polarization, the fluorine anions are expected to form the outer Helmholtz plane, resulting in an accumulation of fluorine anions near the electrode surface.[74] The higher polarizability of anions often leads to the shedding of their solvation shell and specific adsorption which enhances the capacitance under positive polarization. However, fluoride is not a typical anion, and is not very polarizable because it is small. Consequently, it can be solvated in polar solvents.[75]

Similarly, sodium cations are expected to accumulate near the electrode surface when negatively polarized. Cations typically have a stronger solvation shell and do not specifically adsorb. However, if electro-adsorbed, their smaller size can lead to higher capacitance, due to smaller distance of closest approach.[74,76] The residual negative charge of the MoS_2 without any applied bias, due to the chemical reduction of MoS_2 with n-butyllithium, may be capable of stripping the solvation shell and allowing electro-adsorption.

The ratio of the radius of a solvated fluoride ion (0.358 nm)[77] to the radius of an unsolvated sodium ion (0.102 nm)[78] is 3.51 whereas the drop in capacitance ratio observed is between 2.4 and 4.5 depending on the value of the capacitance chosen in the sloping positive polarization branch of the potential-dependence. Thus, the ratio fits, although, the low capacitance under positive polarization is much smaller than what is typically reported for the capacitance in the Helmholtz layer measured in classic experiments on mercury in aqueous NaF to be ~16-25 $\mu F/cm^2$.

Faradaic reactions may also contribute to the observed potential dependence of 1T MoS_2 resulting in what is known as pseudocapacitance. Such reactions are often a strong function of frequency and thus one might expect the shape of the capacitance-potential plot to change with the frequency plotted.[38] The presence of oxygen during MoS_2 synthesis can result in defects that enhance capacitance in aqueous electrolytes, which are then suppressed in organic electrolytes.[79,80]

Furthermore, the multiple oxidation states of Mo allow for faradaic charge storage in aqueous electrolytes.[80] As shown in Figure 21b, the shape remains the same in the aqueous and organic electrolytes, irrespective of frequency. The magnitude of the capacitance is simply diminished with increasing frequency. Furthermore, upon analyzing the frequency dispersion, no change between 1T and 2H MoS_2 is observed in the range of 10-100 Hz which suggests the absence of slower pseudocapacitive reactions.

4.3.3 Characterization of Monolayer MoS_2 Films in Organic Electrolyte

The MoS_2 electrodes were also tested in an organic electrolyte in an attempt to eliminate the effect that proton transfer reactions between surface functional groups on MoS_2 (for example, the MoO_x defects detected by XPS) and the aqueous electrolyte would have on the capacitance. Figure 21c demonstrates that switching to an organic electrolyte causes the capacitance to drop by nearly a factor of 2. Upon inspecting the entire frequency range in Figure 21, the ratio is approximately 2 until a frequency of 10^4 Hz, at which the measured capacitance in aqueous electrolyte is much smaller. This rapid decrease in the ratio can be attributed to differences RC time constant, which dictate when the plateau in the frequency dependence ends.
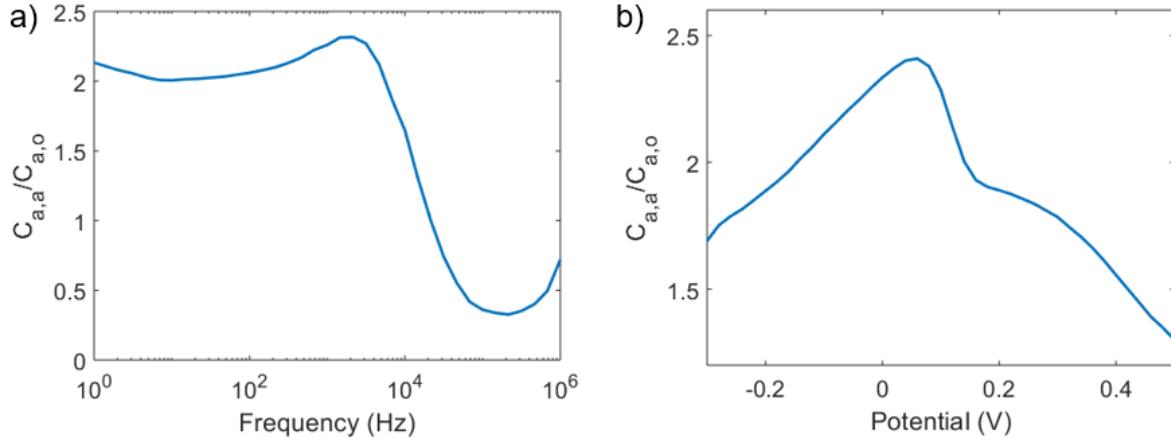
Moreover, at the lower frequencies where Faradaic reactions can occur, the capacitance ratio is relatively constant, suggesting that pseudocapacitance from slower redox reactions is not the cause of the capacitance drop.

As shown in Figure 21d, the change in electrolyte similarly results in a drop by approximately 2 over the entire potential range, with a higher ratio for potentials near 0 V and a lower ratio for more positive or negative potential values. The fact that a similar drop in capacitance was observed over all voltages suggests the high capacitance observed for 1T MoS_2 under negative polarization is not due to redox reaction involving proton transfer. The reduction in capacitance in organic compared to aqueous electrolyte can partially be explained by the Stern theory. The radius of a solvated tetraethylammonium ion is 0.482 nm, while the radius of an unsolvated tetraethylammonium ion 0.4 nm.[81]

The ratio of unsolvated aqueous cationic radius to unsolvated organic cation radius is 4, which is over two times higher than the ratio of measured capacitances at more negative polarizations, where the solvation shell is expected to be stripped. Meanwhile, the ratio of solvated aqueous cationic radius to solvated organic cation radius is 1.35, which almost exactly matches the ratio of measured capacitances at more positive polarizations where the solvation shell is expected to be intact. This strongly suggests that the differences in ion size are the reason behind the drop in capacitance upon changing electrolytes.

Frequency and voltage dependence plots for ratio of capacitance measured in aqueous electrolyte ($C_{a,a}$) to capacitance measured in organic electrolyte ($C_{a,o}$) are shown in Figure 22. Figure 22a shows how the ratio is approximately 2 until a frequency reaches 10^4 Hz, which is
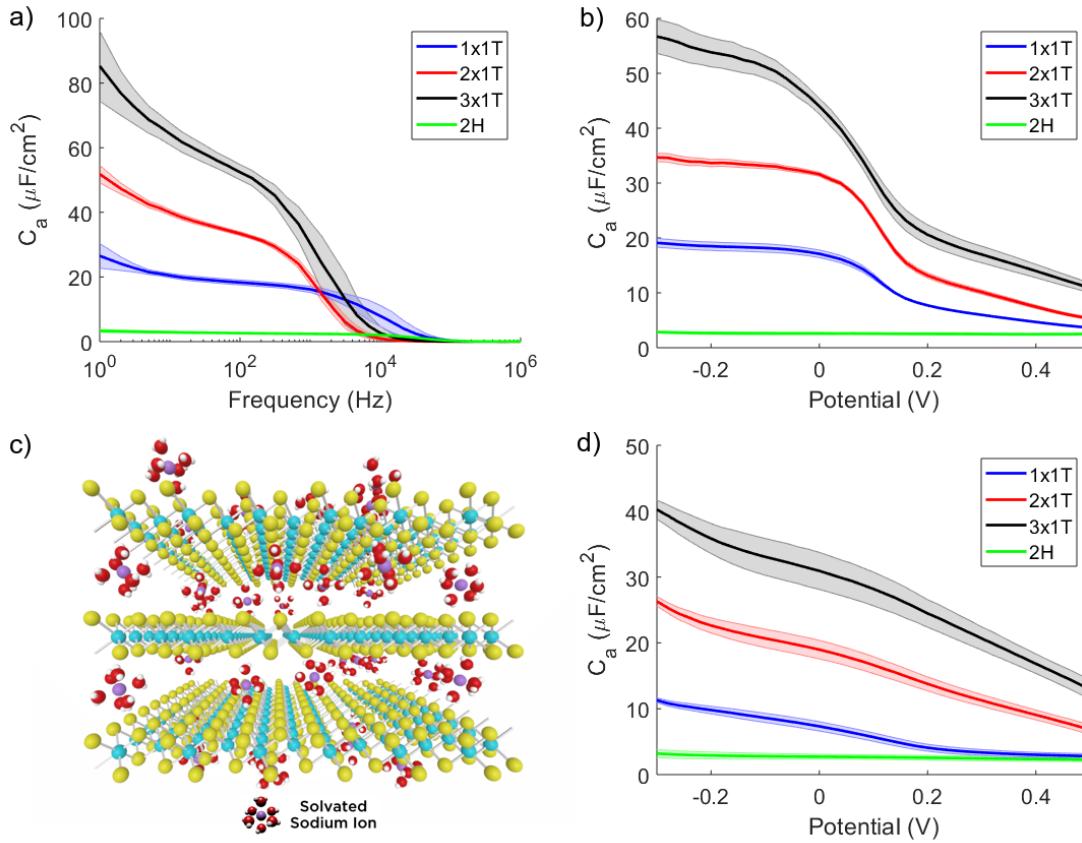
when the plateau of the curve ends. Following this point, $C_{a,a}$ is considerably lower than $C_{a,o}$. Figure 22b shows that the ratio is ~1.75 at -0.3 V, the lowest potential applied, before increasing until reaching a peak of ~2.5 at 0 V, then decreasing to ~1.25 at 0.5 V, the highest potential applied.

Figure 22. Ratio of capacitance in aqueous electrolyte to capacitance in organic electrolyte for monolayer 1T MoS_2 films as a function of a) frequency at -0.14 V and b) potential at 100 Hz
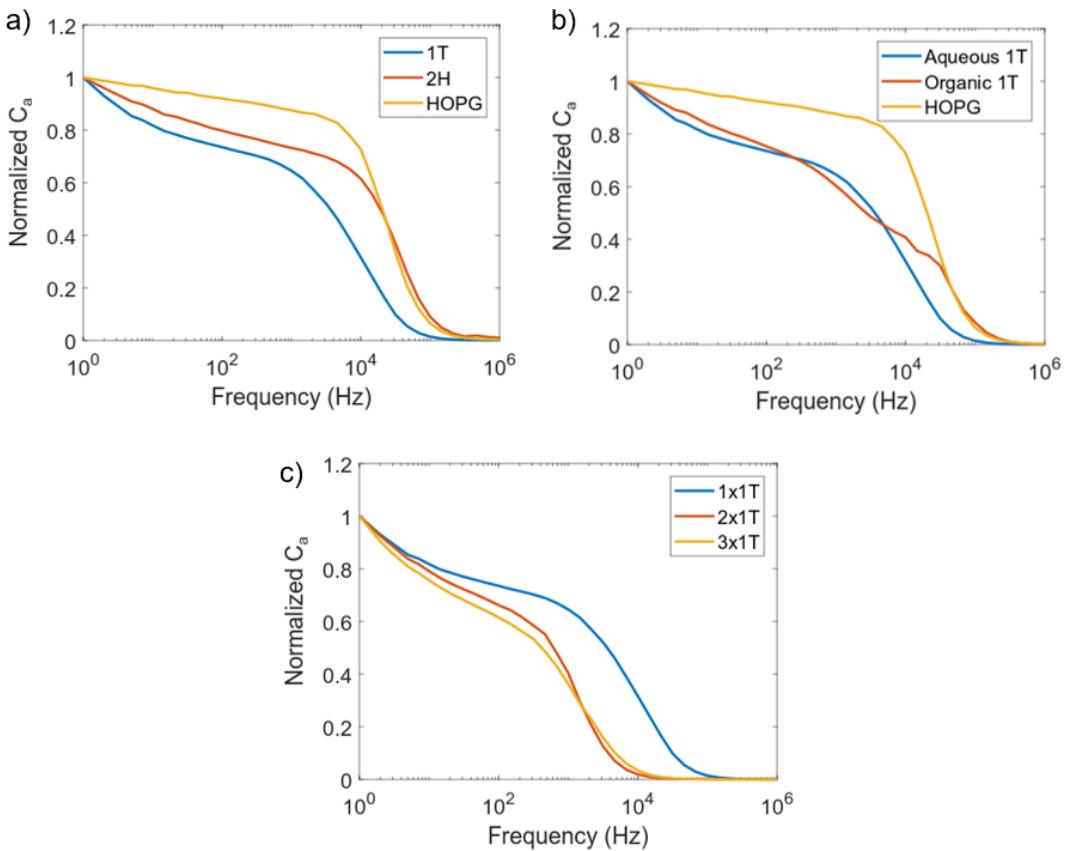
4.3.4 Characterization of Multilayer MoS_2 Films

In order to investigate intercalation effects, the same methods were applied to multilayer MoS_2 electrodes fabricated layer-by-layer using the same 1-layer MoS_2. Figure 23a shows the frequency dependence of multi-layer MoS_2 films. At low frequencies, the capacitance is found to increase linearly with layer number suggesting that ions can access the interlayer galleries between restacked MoS_2. The slope of the low frequency portion of the curve (*i.e.*, the frequency dispersion) increases slightly with each layer indicating that charging the underlying layers takes place over a longer time-scale.

Figure 23. Areal capacitance of multilayer MoS_2 films in aqueous electrolyte as a function of a) frequency at -0.14 V vs. Ag/AgCl (1 M) and b) potential at 100 Hz, c) a schematic diagram of the restacking behaviour of MoS_2, d) areal capacitance of multilayer MoS2 films in organic electrolyte as a function of potential at 100 Hz.

Capacitance frequency plots normalized to unity can be found in Figure 24. Figures 24a and 24c show normalized frequency plots for measurements in aqueous electrolyte, which better show this increased frequency dispersion. Figure 24a shows how the plateau of the curve ends at lower frequencies following the deposition of a 1T MoS_2 electrode. This can be attributed to an increased RC time constant resulting from higher capacitance. Figure 24c demonstrates a similar phenomenon following additional layer depositions. Figure 24b shows a flatter frequency dependence in organic electrolyte, in which the S-shaped curve observed for measurements in aqueous electrolyte becomes almost linear.
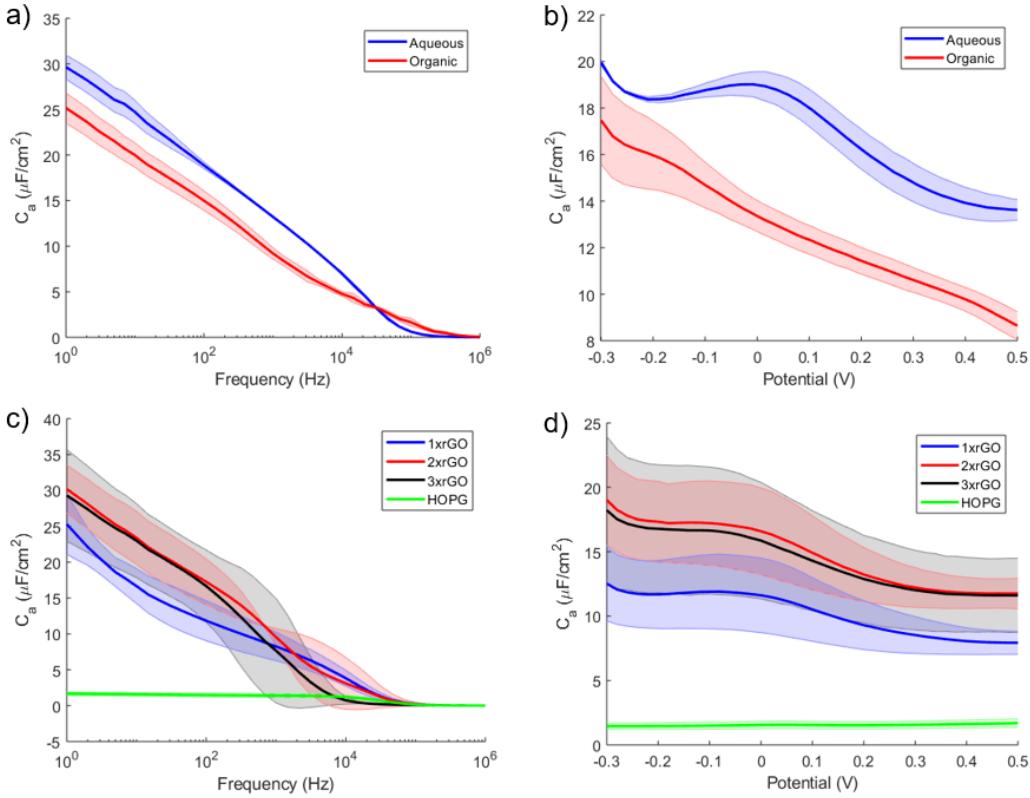
Figure 24. Areal capacitance MoS$_2$ films as a function of frequency at -0.14 V, comparing differences in a) 1T and 2H MoS$_2$, b) aqueous and organic electrolyte, and c) single, double, and triple layer films.

Figure 23b demonstrates the voltage dependence of the multi-layer MoS$_2$ films obtained at 100 Hz. The capacitance of the films increases almost linearly with layer over nearly the entire potential range. This suggests that ions can intercalate between re-stacked sheets, as demonstrated previously,[13] but also that this is independent of potential unlike more typical intercalation reactions which occur at some defined redox potential. Figure 23c illustrates how the restacking of MoS$_2$ still allows for ion intercalation between the nanosheets, resulting in layer-dependent capacitance behaviour.

Additionally, the capacitance of multilayer MoS_2 was investigated in organic electrolyte, as shown in Figure 23d. The general patterns observed in aqueous electrolyte were also observed upon addition of multi-layers. When it comes to double and triple layer films, the continuous increase in capacitance, suggests that the organic electrolyte is still able to intercalate the MoS_2 layers. Therefore, the decrease in capacitance of a MoS_2 monolayer observed by switching from aqueous to organic electrolyte cannot by attributed to restacking layers. Rather, it is more likely caused by larger ion size. Moreover, this provides evidence for the previously made hypothesis that unexfoliated 2H MoS_2 chunks seen in the AFM images do not contribute to the measured capacitance of the monolayer. Previous studies done on MoS_2 supercapacitors also reported a reduction by half after switching to an organic electrolyte from an aqueous electrolyte.[13]

4.3.5 Characterization of rGO Films

For comparison, the same experiments were conducted on rGO films, as seen in Figure 25. First of all, the C/E curve (Figure 25b) lacks the V-shape of thermally reduced graphene oxide monolayers, as reported by several other sources.[39,41,46] This can be attributed to unreacted surface epoxy, hydroxyl, and carboxylic functional groups found on chemically reduced graphene oxide.[38] Such functional groups can cause charge behaviour changes in aqueous electrolytes in response to the potential range.[38] These functional groups are likely also the reason why the measured capacitance decreases substantially in organic electrolyte. Previous work has also demonstrated the lack of a V-shape in the C/E curve with rGO.[38] Furthermore, the Dirac point exhibited by perfect graphene would not be seen in defective, partially oxidized rGO as the bandgap would be greater than zero.[82]

Figure 25. Areal capacitance of rGO films in aqueous and organic solvents as a function of a) frequency at -0.14 V and b) potential at 100 Hz. Areal capacitance of monolayer and multilayer rGO films as a function of c) frequency at -0.14 V and d) potential at 100 Hz.
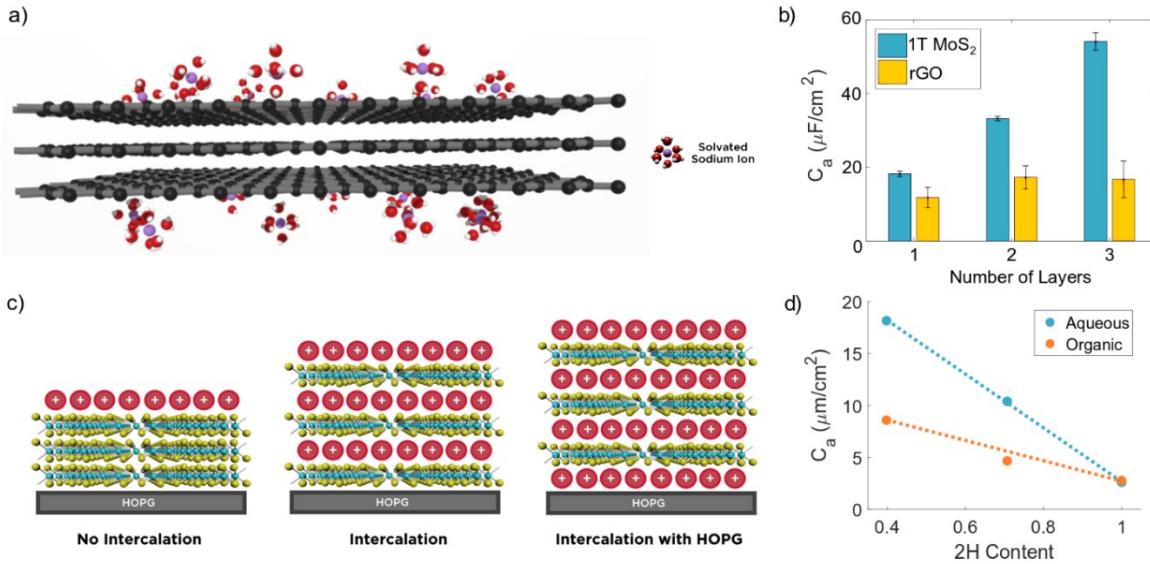
The measured specific capacitance values of 8-12 µF/cm^2 at 100 Hz are considerably higher than the values of 5-8 µF/cm^2 reported by Xia et al. and 5-6 µF/cm^2 reported by Stoller et al. This increase is likely caused by the presence of functional groups, whereas the work of both Xia et al. and Stoller et al. deals with pristine, defect-free graphene.[41] Conversely, previous work, which involved measuring the intrinsic capacitance of defect-rich rGO, demonstrated specific capacitance values of 12-17 µF/cm^2.[42] The noticeably higher values can be attributed to more complete reduction of GO through a thermal, rather than chemical, reduction method[38].

Next, the capacitance behaviour of multilayer rGO was investigated to determine the restacking behaviour of rGO. The frequency dependence plot in Figure 25c shows similar curves

for the multilayer samples, but a drastically different shape for the monolayer sample. Monolayer rGO films show a slight upturn in capacitance at frequencies less than 10 Hz, which is not present in multilayer rGO samples. Some faradaic processes occur at slower rates,[42] suggesting that the contribution of such reactions is diminished upon the deposition of a second layer of rGO.

Moreover, measurements made on the rGO samples show considerably higher standard deviation than those on the MoS_2 samples, perhaps indicating non-uniformity in either the layer number or extent of reduction in each deposited layer. The voltage dependences of the multilayer samples (Figure 25d) are similar to each other, yet distinct from the monolayer samples. The capacitances of the rGO multilayer samples range from 12 to 20 $\mu F/cm^2$ between -0.3 to 0.5 V. Unlike the results obtained for 1T MoS_2 multilayer films, the capacitance of multilayer rGO films does not scale with layer number.

The capacitive behaviour of multilayer rGO was investigated to determine the restacking behaviour of rGO and compare it to that of 1T MoS_2. While the addition of a second layer causes a noticeable increase in the capacitance, the deposition of a third layer has no further effect. This is because graphene nanosheets aggregate and restack when layered on top of each other, reducing accessible specific surface area and decreasing gravimetric/volumetric capacitance.[37] Figure 26a illustrates how the restacking of rGO nanosheets prevents ion intercalation. This is in contrast to the behaviour of multilayer MoS_2 electrodes, which show continuous increase in capacitance with layer number, as shown in Figure 26b. This can potentially be attributed to differences in interlayer spacing between graphene and MoS_2. While the carbon-carbon interlayer distance of graphene is reported as 0.142 nm,[14] the interlayer spacing of restacking MoS_2 is 0.615 nm.[18]

Figure 26. Schematic diagram of the restacking behaviour of rGO, b) areal capacitance plotted against number of layers for both 1T MoS₂ and rGO multilayer electrodes, c) a schematic diagram illustrating the various possible charging mechanisms, and d) measured areal capacitance at 100 Hz and -0.14 V vs. Ag/AgCl (1 M) plotted against 2H content

4.3.6 Comparison of Experimental Measurements to Theoretical Predictions

The measured capacitance of each MoS₂ sample will now be compared to what we might expect from theory for pure phase 1T and 2H MoS₂ based on theory for semimetals and semiconductors, respectively. The intrinsic capacitance of both materials is calculated and compared with the measured values at the OCP (-0.14 V), which is expected to be approximately the pzc. 2H MoS₂ is assumed to be a semiconductor, and the space charge capacitance for the pzc is calculated based on the charge carrier concentration (n): $C_{SC} = \left[\frac{2\varepsilon\varepsilon_0 e^2 n}{kT}\right]^{0.5}$ where ε is the relative permittivity of MoS₂ (3.7)[83] and ε_0 is the permittivity of vacuum.[43,44,84] Previously, a charge carrier concentration of 7.36×10^{16} cm⁻³ was measured by Lee *et al.* for MoS₂ thin films, and this value is used in the calculations.[85] This leads to an estimated $C_{SC,2H}$ = 0.548 μF/cm². On the other hand, Gerischer's relationship is used to predict the capacitance of a semi-metallic 1T phase as a

function of the DOS (N_0) near the Fermi energy: $C_{SC} = \sqrt{\varepsilon\varepsilon_0 N_0 e}$, where e is the charge of an electron.[39] The DOS is calculated to be 1.367×10^{22} eV^{-1} cm^{-3}, which is in good agreement with the values reported by Wang *et al.*[86] This leads to an estimated $C_{SC,1T}$ = 25.2 µF/cm^2.

While ions have been shown to intercalate 1T MoS$_2$ nanosheets, it is uncertain whether charge is stored solely on the exposed side of the film ('No Intercalation') or if ions can penetrate between the film and the substrate which could cause double-layer charging on both sides of MoS$_2$ ('Intercalation') as well as exposing additional HOPG to the electrolyte ('Intercalation with HOPG'). Figure 26c illustrates each case of charging behaviour considered. The expected intrinsic capacitance in each of these cases is calculated and compared with measured results. To calculate the intrinsic capacitance (C_a), the space charge capacitance (C_{SC}), Helmholtz capacitance (C_H), and diffuse double layer capacitance (C_{diff}) are combined according to the work of Gerischer.[45] This involves the use of Equation 1 from Chapter 2, with a Helmholtz capacitance of 25 µF/cm^2 for the aqueous electrolyte[10] and 11 µF/cm^2 for the organic electrolyte[87].

The capacitance of a monolayer MoS$_2$ electrode with intermediate 2H content was also measured. Capacitance values at the OCP are plotted against measured 2H content, in Figure 26d. These data are used to extrapolate expected capacitance values for 'pure phase' 1T and 2H MoS$_2$ monolayer electrodes. When considering the cases assuming intercalation, the measured value is divided by 2 to account for the doubling of surface area with both sides exposed. Therefore, the experimental value of pure phase 1T MoS$_2$ would be reduced from 29.8 to 14.9 µF/cm^2, while it would be reduced from 2.7 to 1.35 µF/cm^2 for 2H MoS$_2$ in aqueous electrolyte. Table 2 shows the comparison of values calculated from theory and values obtained from EIS and CV measurements.

EIS values are taken from measurements, while CV values are first calculated from Equation 3, as follows:

$$C = \frac{\int IdV}{v \times A \times \Delta V} \ (3)$$

where $\int IdV$ is the area under the CV curve, v is the scan rate (100 mV/s), A is the exposed area of the electrochemical cell, and ΔV is the potential stability window (0.8 V). However, since calculations made with EIS measurements only examined values at the open circuit potential (-0.14 V), a second calculation is made using Equation 4, as follows:

$$C = \frac{\Delta I_{OCV} \Delta V}{v \times A \times \Delta V} = \frac{I_{OCV}}{v \times A} \ (4)$$

where ΔI_{OCV} is the difference in current values recorded at the open circuit potential. These values are denoted as CV@OCV.
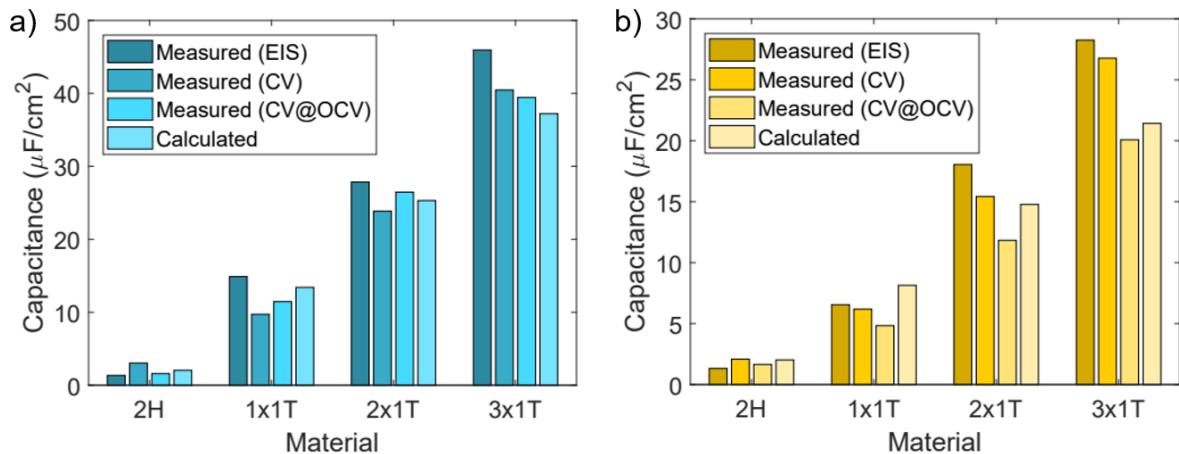
Table 2. Measured and calculated intrinsic capacitance values for 1T and 2H MoS$_2$ in aqueous and organic electrolyte

	Measured (EIS)		Measured (CV)		Measured (CV@OCV)		Calculated	
	Aqueous	*Organic*	*Aqueous*	*Organic*	*Aqueous*	*Organic*	*Aqueous*	*Organic*
1x1T	14.90	6.55	9.72	6.19	11.46	4.83	13.41	8.14
2x1T	27.85	18.05	23.87	15.43	26.46	11.83	25.31	14.78
3x1T	45.95	28.25	40.46	26.77	39.45	20.08	37.22	21.42
2H	1.35	1.32	3.04	2.08	1.58	1.65	2.04	2.02

Figures 27a and 27b summarize the comparison between measured and calculated values of the intrinsic capacitance at the open circuit potential under assumptions for the 'Intercalation with HOPG' case, which provide the best match between values. They compare calculated values for monolayer, double layer, and triple layer 1T MoS$_2$ films against their measured values, for

aqueous and organic electrolyte, respectively. Since the capacitance of multilayer electrodes increased substantially with layer number, the case of 'No Intercalation' was rejected.

Similar to EIS values, the CV capacitances are corrected for 1T/2H phase composition. Figure 27 compares the different measured and calculated values in a bar chart. In general, the measured values from CV are slightly lower than that of EIS for 1T MoS_2, and slightly larger for 2H MoS_2. When it comes to measurements in aqueous electrolyte, there are generally higher capacitances calculated for CV@OCV values than for CV values due to the shape of the CV curve being slightly wider at more negative capacitance values. Conversely, for measurements in organic electrolyte, the CV@OCV values are generally lower since the shape of the CV curve is more uniform. Any discrepancy between the EIS values and CV values is caused by the fact that that voltage dependence of the EIS curves is much more significant compared to that of the CV curves, resulting in much higher capacitances recorded for negative potentials. Regardless, good agreement is observed between EIS values and values calculated from theory.

Figure 27. Measured (from EIS and CV) and calculated intrinsic capacitance values compared for 1T and 2H MoS2 in a) aqueous and b) organic electrolyte

When comparing the extrapolated pure phase capacitance measurements in both aqueous and organic electrolyte with calculated values assuming intercalation with HOPG contribution, good agreement is observed in all cases. Deviations between values can be attributed to either experimental error or the presence of oxygen defects which can increase the capacitance through pseudocapacitive contributions.

4.3.7 Theoretical Capacitance Limits

The experimental intrinsic capacitance values for monolayer 1T and 2H MoS$_2$ can be used to calculate theoretical gravimetric and volumetric capacitance limits for supercapacitors made with these materials. When multiplying the obtained $C_{a,1T}$ = 14.9 µF/cm^2 from measurements in aqueous electrolyte with 636 m^2/g, the specific surface area of MoS$_2$, we arrive at 94 F/g, the theoretical gravimetric capacitance.[17] By further multiplying the value with 5.06 g/cm^3, the density of MoS$_2$, we arrive at 479 F/cm^3, the theoretical volumetric capacitance.[88]

This value falls within the volumetric capacitance range of 400-650 F/cm^3 reported by Acerce at al. for their 1T MoS$_2$ nanosheet supercapacitor in aqueous electrolyte.[18] Furthermore, by using the obtained $C_{a,1T}$ = 6.55 µF/cm^2 from measurements in organic electrolyte, we arrive at theoretical gravimetric and volumetric capacitances of 42 F/g and 211 F/cm^3, respectively. The latter value almost perfectly matches the volumetric capacitance Acerce *et al.* reported for measurements in TEABF$_4$/ACN of 199 F/cm^3.[18]

Similar calculations for 2H MoS$_2$ predict a gravimetric and volumetric capacitance limit of 8 F/g and 42 F/cm^3, respectively in both electrolytes. The performance of 1T MoS$_2$ supercapacitors appears to be at the theoretical volumetric capacitance limit. Therefore, to further

improve capacity, one must consider introducing other materials,[1] incorporating defects which enable pseudocapacitance,[79] or producing asymmetric supercapacitors, in which MoS_2 is used as the negative electrode due to the significantly higher capacitance observed under negative polarization.[32] Further work is required to determine the reason why the intrinsic capacitance of the 1T polymorph/electrolyte interface approaches that of the 2H polymorph at potentials significantly larger than the pzc.

4.4 Conclusion

In this chapter, the charge storage mechanisms and intrinsic capacitance of MoS_2 and rGO are investigated. By examining the behavior of multilayer MoS_2 and rGO electrodes, it was apparent that MoS_2 nanosheets restack in a way which allows for ion penetration between nanosheets, resulting in layer dependent capacitance. Conversely, rGO nanosheets restack so that ion accessible surface area is reduced, resulting in layer independent capacitance.

In aqueous electrolyte, the intrinsic capacitances of 1T MoS_2 and 2H MoS_2 were found to be 14.9 and 1.35 $\mu F/cm^2$, respectively, showing a tenfold difference. However, this appears to only be the case at more negative potentials. At positive potentials, the S-shaped voltage dependence of 1T MoS_2 showed capacitance values which approached that of 2H MoS_2. The complex voltage dependence of 1T MoS_2 can potentially be attributed to pseudocapacitance, or Stern layer effects.

In organic electrolyte, the intrinsic capacitance for 1T MoS_2 was found to be 6.55 $\mu F/cm^2$, approximately half the value obtained from measurements in aqueous electrolyte. This can be explained by the larger organic electrolyte ions being unable to pack as efficiently. While the change for 1T MoS_2 was very large, the change for 2H MoS_2 was very small. This suggests that

while 2H MoS_2 is limited by space charge capacitance, 1T MoS_2 is limited by Helmholtz capacitance.

The intrinsic capacitance was extrapolated to determine an upper limit for the capacitance of MoS_2 supercapacitors. For supercapacitors with aqueous and organic electrolytes, the volumetric capacitance limits are 479 F/cm^3 and 211 F/cm^3, respectively. These values are in good agreement with some of the highest recorded values for volumetric capacitance and suggest that pure MoS_2 supercapacitors have reached the limit.

Chapter 5: Defect Engineering of MoS$_2$ Nanosheets

5.1 Introduction

At the end of Chapter 4, it becomes apparent that the upper limit of capacitance for pure MoS$_2$ supercapacitors has been reached. Therefore, changing the architecture of MoS$_2$ supercapacitor devices should no longer result in significant capacity increases. Instead, efforts should be focused on either MoS$_2$-composite materials or defect engineering of MoS$_2$ nanosheets. In this chapter, two types of defects are introduced into MoS$_2$ nanosheets: sulfur vacancies and edge sites.
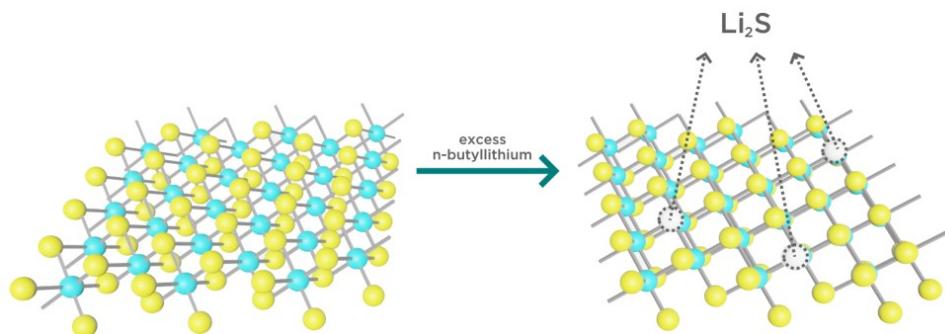
Sulfur vacancies were introduced by increasing the amount of lithium intercalant used during MoS$_2$ exfoliation, while edge sites were produced by decreasing lateral flake size via probe sonication. Various characterization techniques, such as EDS and dynamic light scattering (DLS) were leveraged to determine the extent of nanosheet defectiveness. Once sufficiently defective nanosheets were synthesized, Langmuir films of the materials were deposited. Then, CV and EIS of the monolayer electrodes were once again employed to determine the intrinsic capacitance of the materials.

5.2 Experimental

5.2.1 Defect Engineering
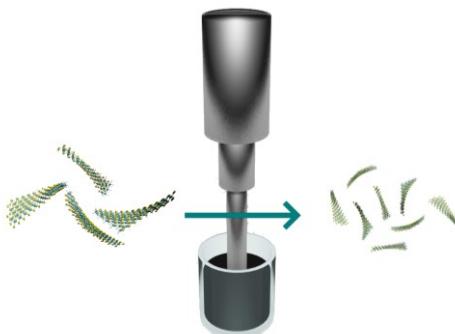
Defect engineering was studied in two ways: the introduction of sulfur vacancies and the creation of edge sites. Previous studies have shown that sulfur vacancies and edge sites increase the hydrogen evolution reaction catalytic activity, but not the intrinsic capacitance.[15] In liquid

exfoliation methods, lithium intercalation can induce the formation of sulfur vacancies via the precipitation of Li_2S from MoS_2, as shown in Figure 28.[89] To change the density of sulfur vacancies, the ratio of bulk MoS_2 to n-butyllithium (n-ButLi) used in the lithium intercalation reaction was varied. For 5 mL of n-ButLi, the reaction was carried out with 0.125 g, 0.25 g, and 0.5 g of bulk MoS_2 powder. These samples are denoted as 3xButLi, 2xButLi, and 1xButLi, respectively, and in general as the ButLi samples.

Figure 28. Schematic diagram of sulfur vacancy formation.

Edge sites are created in MoS_2 through the reduction of lateral size via probe sonication of nanosheet suspensions, as shown in Figure 29. Sonication was carried out continuously for periods of 0.25 hours and 1 hour at 70% power, then the capacitances of the resulting samples were measured and compared to that of unsonicated samples. In general, these samples will be referred to as the sonicated samples.

Figure 29. Schematic diagram showing use of sonication to reduce lateral flake size.

60

5.2.2 Characterization

To estimate the atomic fraction of sulfur vacancies in the nanosheets, EDS using an SEM (LEO 1550, Zeiss) was conducted on MoS_2 dispersions drop cast onto Si wafers. The EDAX TEAM™ EDS System for the SEM was used for elemental analysis. The ratio of the atomic percentages of sulfur to molybdenum was calculated, and the percent deviation from 2, the expected atomic ratio, was taken as the percentage of sulfur vacancies. To distinguish the contribution of sulfur vacancies to the capacitance from that of changes in 1T/2H phase composition, UV-Vis absorption spectra were obtained using a SpectraMax M2 Microplate Reader with cuvette port to calculate the 1T/2H ratio and extrapolate the capacitance for a 100% 1T sample. Raman spectra were also obtained to observe any additional effects on the MoS_2 by changing n-ButLi content.

To estimate the size and number density of edge sites, the lateral size was taken as the Z-average hydrodynamic radius measured through DLS. Reduction in size following sonication was further verified by analysis of AFM images taken with a Digital Instruments Nanoscope IV. UV-Vis and Raman spectra were also obtained to ensure that only edge site density was affected by sonication. Optical microscopy of all monolayer MoS_2 films on Si/SiO_2 substrates was used to qualitatively access film quality. AFM images were once again analyzed using the Python script to quantitatively access total coverage fractional coverage by layer number.

For electrochemical characterization, the same three-electrode electrochemical cell was used with 1 M NaF in water as the chosen electrolyte. An Ag/AgCl reference electrode (1 M) and Pt wire counter electrode (0.5 mm diameter, 99.99% purity) were used. Cyclic voltammetry (CV)

and electrochemical impedance spectroscopy (EIS) were conducted in a voltage window of -0.5 to 0.5 V, with nitrogen bubbling to prevent the formation of superoxides.

This voltage window was chosen because apparent faradaic reactions occur at voltages greater than 0.5 V and less than -0.5 V. In order to prevent redox reactions associated with oxygen, nitrogen was bubbled through the electrolyte. Potential dependence was typically plotted at 100 Hz to eliminate slower Faradaic charging processes from the measurement while frequency dependence was plotted at -0.10 V vs. Ag/AgCl (1 M), the approximate open circuit potential of all coated samples.
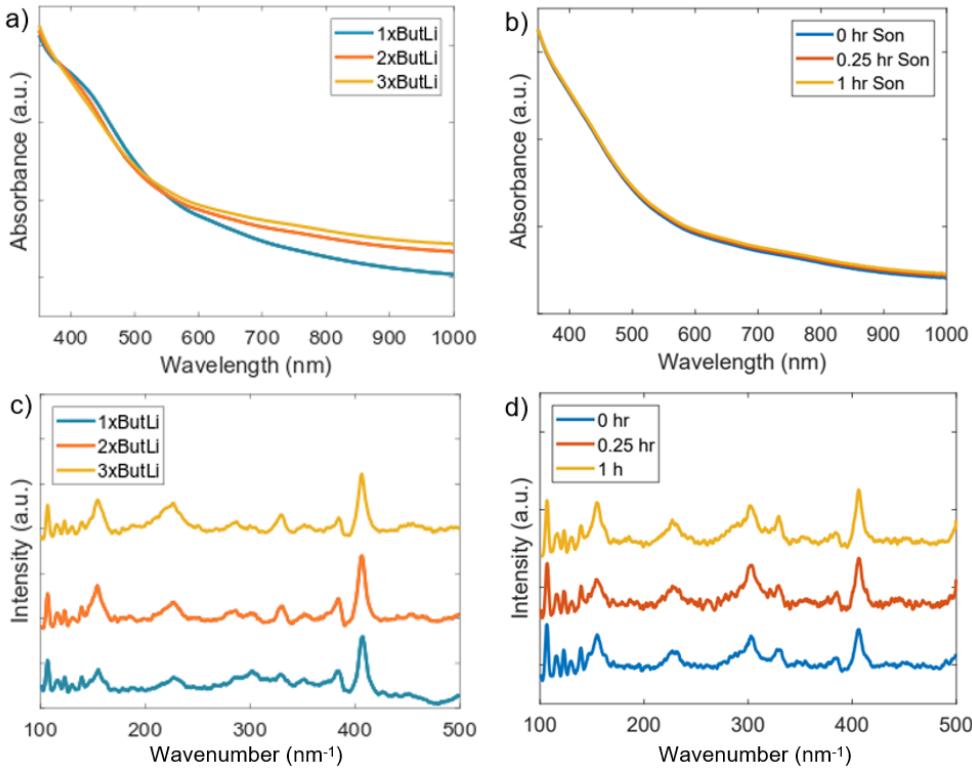
5.3 Results

5.3.1 Characterization of Defect Engineered MoS$_2$ Nanosheets

Normalized UV-Vis spectra from 350 nm to 1000 nm for the ButLi samples can be found in Figure 30a. From the spectra, it can be noted that a primary indicator of the 2H phase, the hump located at 410 nm, decreases in size with increased ButLi content. This indicates that a greater portion of nanosheets are 1T phase, rather than 2H phase. By using Equation 2 from Chapter 3, we can use the ratio of UV-Vis absorbance at 350 nm and 410 nm to calculate the 2H/(1T+2H) ratio. The results of the calculation can be seen in Table 2, which show that the 2H phase decreases with increasing ButLi content. Similar measurements carried out for sonicated samples resulted in relatively little change in phase composition, as shown in Figure 30b.

Table 3. 1T/2H phase composition of MoS$_2$ nanosheets intercalated with varying n-ButLi content

	1xButLi	2xButLi	3xButLi
2H/(1T+2H)	0.425	0.386	0.352

Figure 30. UV-Vis absorption spectrum obtained for monolayer MoS_2 a) intercalated with varying amounts of n-ButLi and b) sonicated for varying durations of time. Raman spectroscopy spectrum obtained for monolayer MoS_2 c) intercalated with varying amounts of n-ButLi and d) sonicated for varying durations of time.
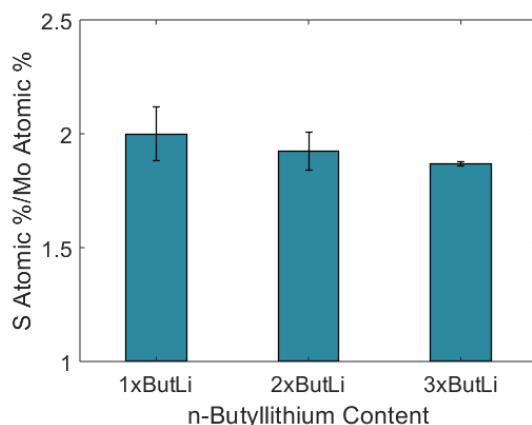
Raman spectroscopy results for ButLi samples are shown in Figure 30c and were used to observe any further changes in the MoS_2 following intercalation with different amounts of n-ButLi. The most prominent peaks can be observed at ~382 cm^{-1} (E^1_{2g}) and ~407 cm^{-1} (A^1_g), which are vibrational modes respectively associated with in-plane and out-of-plane vibrations of 2H MoS_2.[17] No noticeable broadening or shifting of these peaks is observed.

In all samples, three characteristic peaks are observed at 154 cm^{-1}, 226.1 cm^{-1}, and 326.4 cm^{-1}, also known as the J_1, J_2, and J_3 peaks. These peaks, indicative of 1T MoS_2, are enhanced as n-ButLi content increases, suggesting further transformation into the 1T phase.[17] A peak also exists at 227 cm^{-1}, known as the LA(M) peak, which has also been attributed to vacancies and

increased disorder in the system. As n-ButLi content increases, the ratio of the LA(M) peak to the A^1_g peak increases from 0.19 to 0.25 to 0.50, suggesting increased MoS$_2$ disorder.[90]
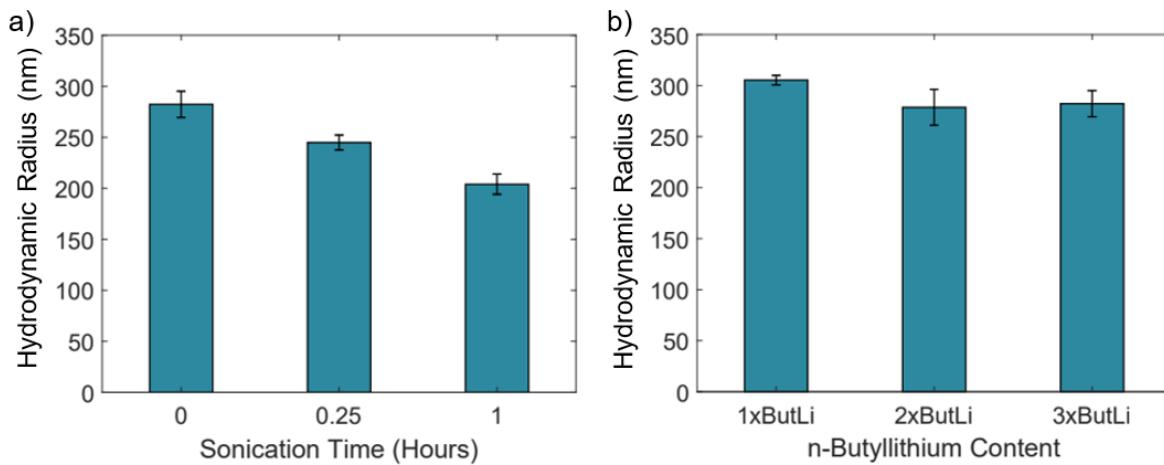
Similarly, Raman spectroscopy results for sonicated samples are shown in Figure 30d and used to detect any further changes in the MoS$_2$ following probe sonication for various durations of time. In agreement with results obtained for ButLi samples, the most prominent peaks are the E^1_{2g} and A^1_g peaks, as well as the J_1, J_2, and J_3 peaks. The intensity of the latter peaks, indicative of 1T MoS$_2$, is unaffected by sonication, suggesting no change in phase.[17] With increased sonication, the ratio of the LA(M) peak to the A^1_g peak changes from 0.42 to 0.38 to 0.37, suggesting little change in MoS$_2$ disorder.[90]

The density of defects found in MoS$_2$ dispersions exfoliated with varying ButLi content was calculated using the S:Mo atomic ratio measured through EDS, as shown in Figure 31. Upon doubling, then tripling the amount of n-ButLi used during intercalation, this atomic ratio decreased from 2 to 1.923 to 1.858. Percent deviation from the expected atomic ratio of 2 is taken as the percentage of sulfur vacancies. This results in calculated sulfur vacancy percentages of 0%, 3.8%, and 6.6%, respectively. Errors bars indicate the standard deviation of each sample.

Figure 31. EDS-measured stoichiometry of MoS$_2$ dispersions intercalated with varying n-ButLi content

Hydrodynamic radius measurements obtained through DLS are shown in Figure 32a. As expected, the hydrodynamic radius, which is approximated as the lateral flake size, decreases as sonication time increases. Unsonicated flakes have an average size of 282.3 ± 10.5 nm, which decreases to 244.9 ± 6.0 nm after 0.25 hours of sonication, and to 204.0 ± 8.1 nm after hour of sonication. Conversely, no clear change in average hydrodynamic radius is measured for the But Li samples, as seen in Figure 32b. Upon increasing the amount of n-ButLi used, the average hydrodynamic radius changes from 305.4 ± 4.6 nm, to 278.7 ± 17.7 nm, to 282.3 ± 10.5 nm, showing no consistent change.
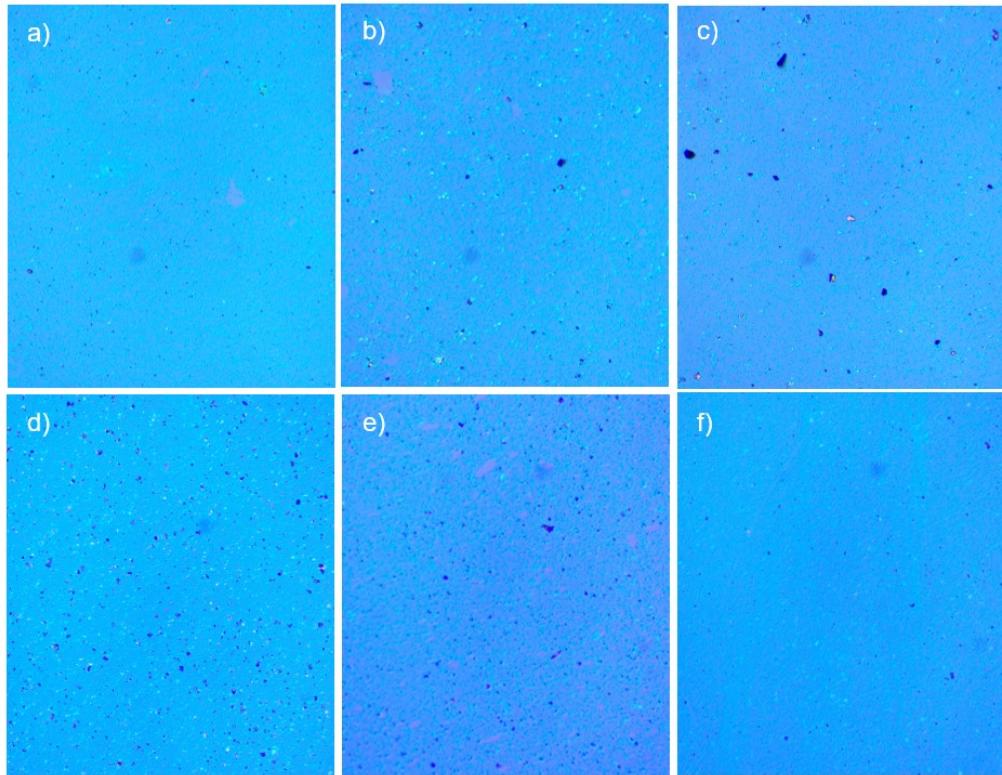
Figure 32. Hydrodynamic radius measured after a) probe sonication for varying durations of time and b) intercalation with varying amounts of n-butyllithium

5.3.2 Characterization of Defect Engineered MoS$_2$ Films
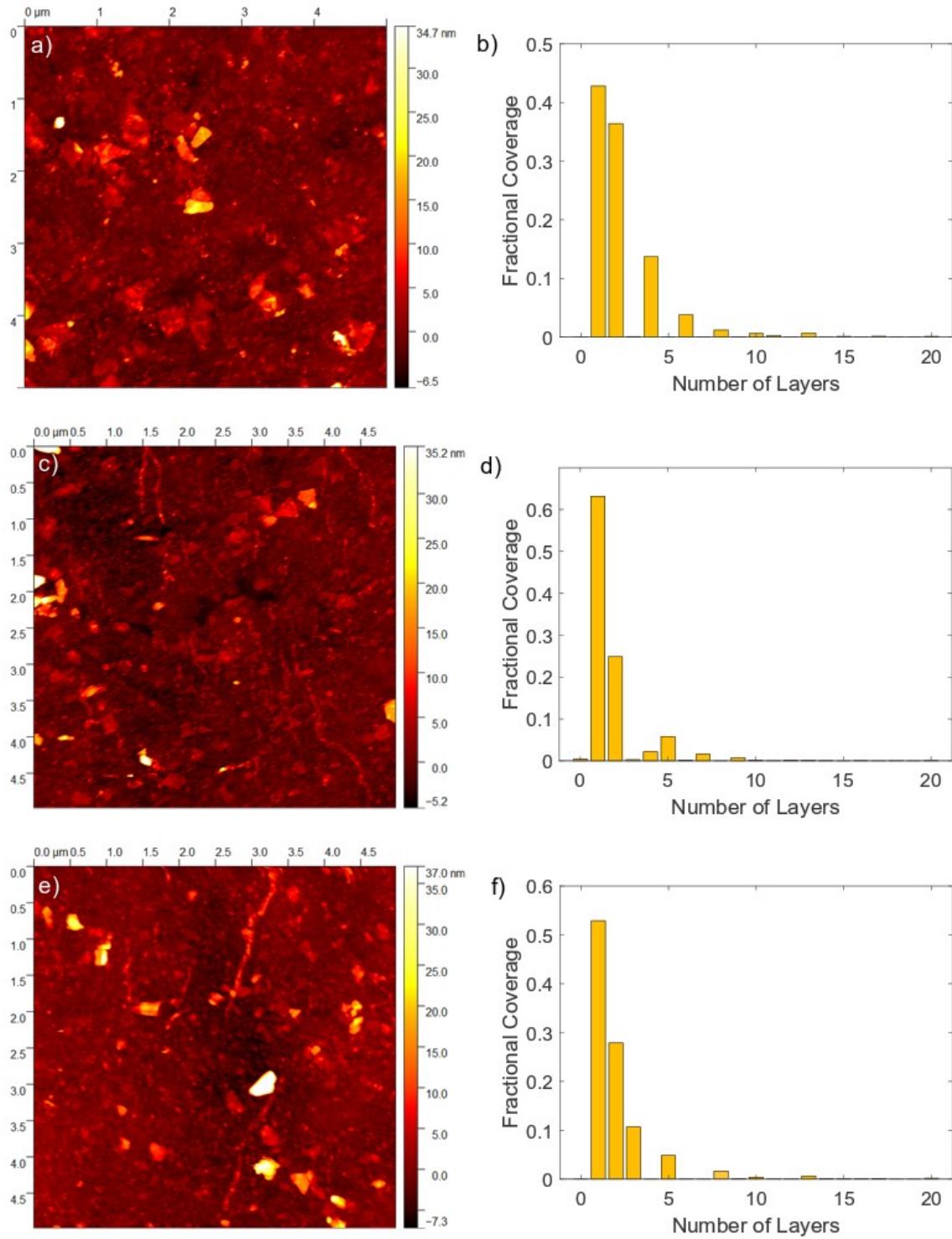
Optical microscopy images of monolayer MoS$_2$ films deposited onto SiO$_2$/Si are shown in Figure 33, demonstrating high coverage. The substrate itself is light purple, while the MoS$_2$ film appears blue, with increasing colour intensity for thicker films. Layer thickness appears to decrease with higher ButLi ratio, which can be attributed to more complete exfoliation of bulk MoS$_2$ powder. This is confirmed through UV-Vis spectroscopy of MoS$_2$ deposited onto glass

substrates. Transmittance measured at 550 nm has been previously shown to decrease with layer thickness. With 1xButLi, 2xButLi and 3xButLi, transmittance decreased continuously. This value is used to normalize capacitance measurements carried out later.
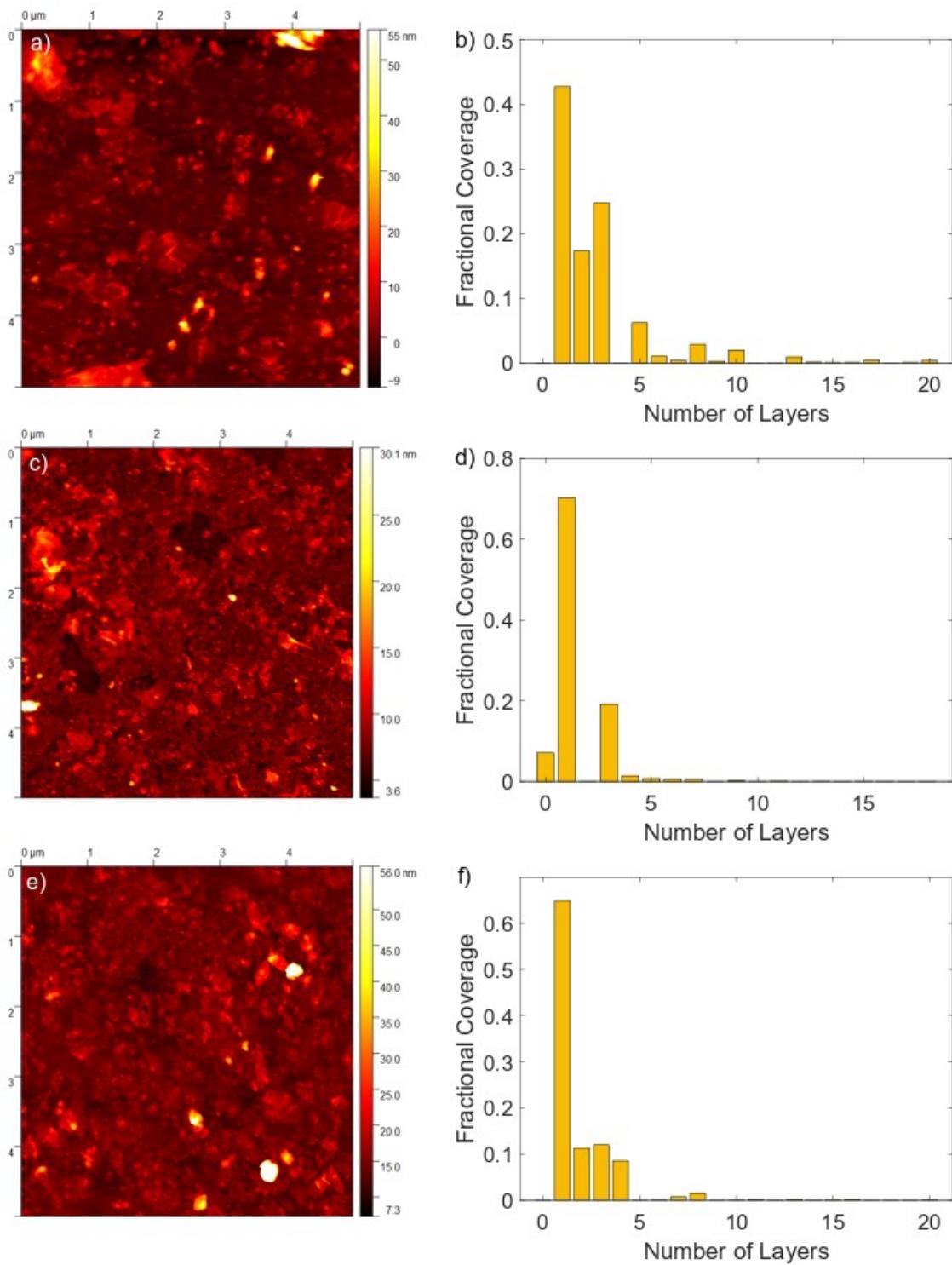
Figure 33. Optical microscopy images of monolayer MoS2 film formation on SiO2/Si wafers for samples intercalated with a) 1xButLi, b) 2xButLi, and c) 3xButLi, and samples sonicated for d) 0 hours, e) 0.25 hours, and f) 1 hour.

AFM images similarly demonstrate a high degree of coverage for sonicated samples, as shown in Figure 34. Analysis with a Python script reveals an average coverage of 99.8% with an average layer number of 2. For ButLi samples, as shown in Figure 35, the coverage is similarly high, revealing an average coverage of 97.3%. However, following higher ButLi content, the layer number decreases from 2.65 to 1.98 to 1.46, corroborating UV-Vis data.
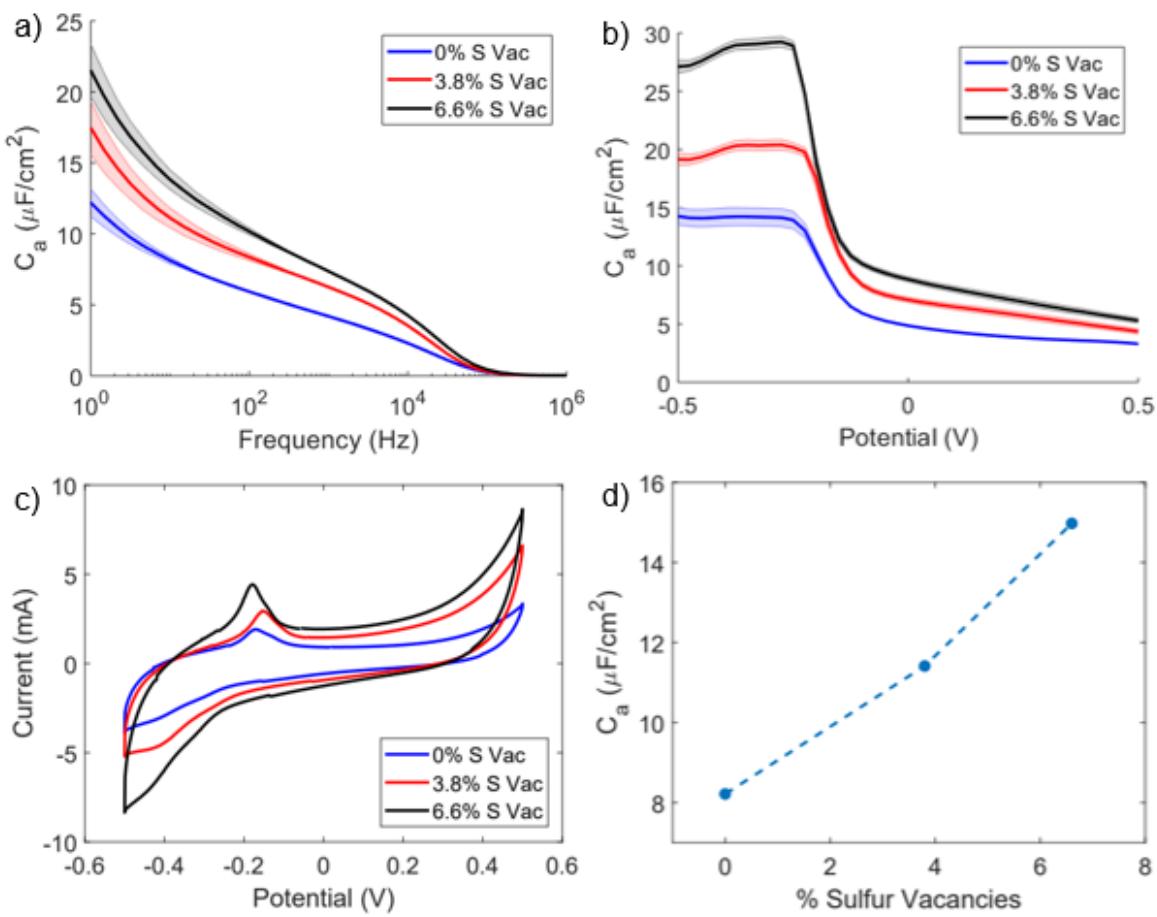
Figure 34. a) AFM image and b) fractional coverage for sample sonicated for 0 hours. c) AFM image and d) fractional coverage for sample sonicated for 0.25 hours. e) AFM image and f) fractional coverage for sample sonicated for 1 hour.

Figure 35. a) AFM image and b) fractional coverage for sample intercalated with 1xButLi. c) AFM image and d) fractional coverage for sample intercalated with 2xButLi. e) AFM image and f) fractional coverage for sample intercalated with 3xButLi.

5.3.3 Electrochemical Characterization of ButLi Samples

Electrochemical characterization of the ButLi samples can be found in Figure 36. The frequency dependence plot in Figure 36a shows that measured capacitance increases with percentage of sulfur vacancies at each frequency, and that no change in the shape of the frequency dependence curves is observed. Figure 36b shows the potential dependence plots, revealing that at all potentials, the capacitance increases with the amount of sulfur vacancies. At about -0.2 V, a sharp drop in the capacitance is observed.

Figure 36. Areal capacitance measured as a function of a) frequency at -0.1 V and b) potential at 100 Hz for ButLi samples. c) Cyclic voltammetry profiles and d) comparison between % sulfur vacancies and intrinsic capacitance for ButLi samples.

Inspection of the cyclic voltammetry profiles for the ButLi samples (Figure 36c) reveals a peak that corresponds to the hump at -0.2 V. Some shift in the potential at which this peak is observed, although no clear relationship between percentage of sulfur vacancies and the peak location is apparent. An assumption can be made that this peak corresponds to increased defectiveness in the MoS_2. To quantitatively assess the effect of increased sulfur vacancies on MoS_2, the intrinsic capacitance is calculated according to the methods discussed in Chapter 4. To account for potential differences in the intrinsic capacitance of 2H MoS_2 (C_{2H}) as a result of sulfur vacancies while extrapolating for 100% 1T MoS_2, a sensitivity analysis is first done assuming different values for C_{2H}, as shown in Table 4. This analysis reveals that potential changes in C_{2H} from 0.6 to 2 $\mu F/cm^2$ would not account for differences in the intrinsic capacitance of the ButLi samples. Figure 36d demonstrates the relationship between percentage of sulfur vacancies and intrinsic capacitance, assuming C_{2H} = 1.3 $\mu F/cm^2$, showing a clear positive correlation.
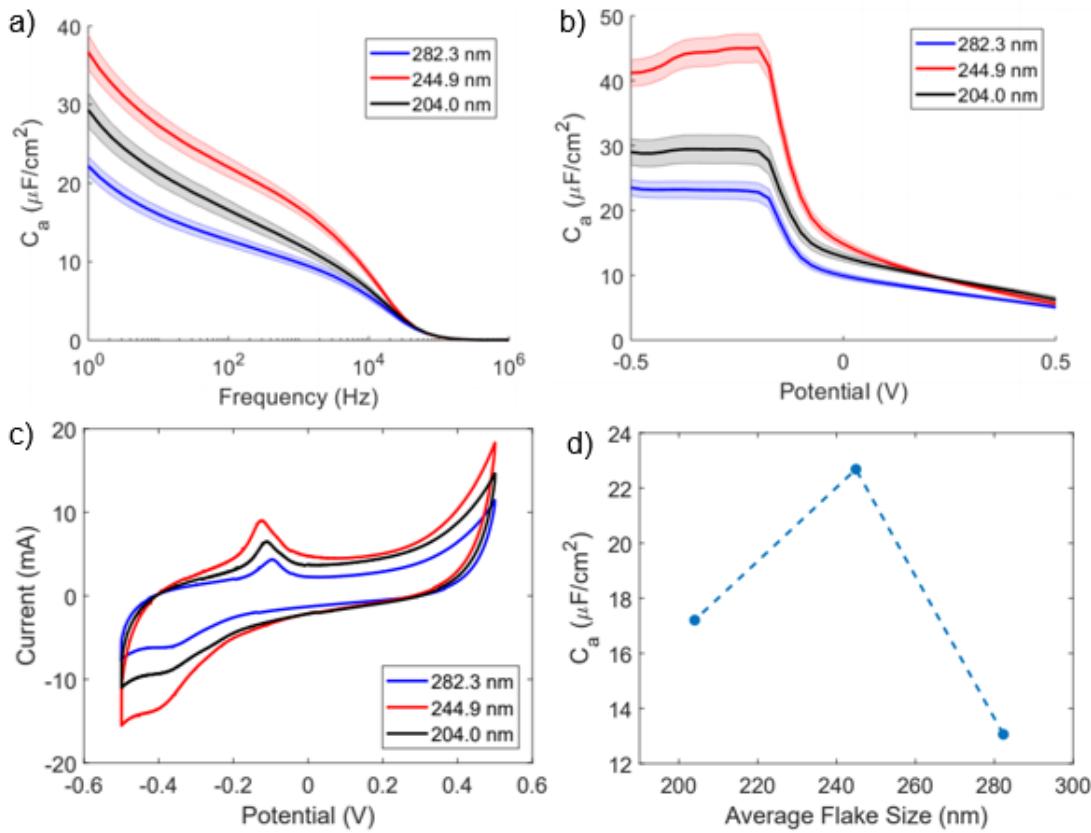
Table 4. Sensitivity analysis for intrinsic capacitance ($\mu F/cm^2$) extrapolation of ButLi samples

C_{2H}	1x ButLi	2x ButLi	3x ButLi
0.6	8.7338	11.854	14.596
1.3	8.2157	11.413	14.976
2	7.6976	10.972	15.356

5.3.4 Electrochemical Characterization of Sonicated Samples

Electrochemical characterization of the sonicated samples can be found in Figure 37. The frequency dependence plot in Figure 37a shows that measured capacitance has a more complicated relationship in response to average flake size. While the capacitance increases following a decrease in flake size from 282.3 nm to 244.9 nm for all frequencies, this relationship does not hold for further size reduction. When lateral size is decreased from 244.9 nm, the measured capacitance

decreases. This turnaround is expected as defects cannot ceaselessly increase capacitance without eventually impairing device performance. This is in agreement with a previous study done on size-dependent electrochemical behavior of MXene flakes, which are few-atoms-thick layers of transition metal carbides, nitrides, or carbonitrides.[91] The potential dependent capacitance behavior followed a similar pattern, also demonstrating the rise of the hump at approximately -0.2 V with increasing measured capacitance. However, as the flake size decreases, the peak is shown to shift towards more positive potentials, moving from -0.2 V to -0.1 V.

Figure 37. Intrinsic capacitance measured as a function of a) frequency at -0.1 V and b) potential at 100 Hz for sonicated samples. c) Cyclic voltammetry profiles and d) comparison between average flake size and intrinsic capacitance for sonicated samples.

Similarly, inspection of the cyclic voltammetry profiles for the sonicated samples (Figure 37c) reveals a peak that corresponds to the hump. A clear relationship exists between the peak potential and the flake size in that smaller flakes cause the peak to be present. Since this peak appears regardless of what type of defect is present, it can further be attributed to general defectiveness of the MoS_2, perhaps due to some Faradaic reaction. To more quantitatively assess the effect of flake size on MoS_2, the intrinsic capacitance is once again calculated. Another sensitivity analysis, shown in Table 5, confirms that potential changes in C_{2H} from 0.6 to 2 $\mu F/cm^2$ would not account for differences in the intrinsic capacitance of the sonicated samples. Figure 37d demonstrates the relationship between flake size, assuming C_{2H} = 1.3 $\mu F/cm^2$, showing an increase in capacitance following the first size reduction, and a decrease in capacitance following the second size reduction.

Table 5. Sensitivity analysis for intrinsic capacitance ($\mu F/cm^2$) extrapolation of sonicated samples

C_{2H}	0 hr Son	0.25 hr Son	1 hr Son
0.6	13.439	23.061	17.585
1.3	13.059	22.681	17.205
2	12.679	22.301	16.825

5.4 Conclusion

In summary, the findings of this chapter show defect engineering allows for the enhancement of intrinsic capacitance in monolayer MoS_2 films. Increasing percentage of sulfur vacancies from 0% to 6.6% induces a continual increase in capacitance. Conversely, while decreasing lateral flake size from 282.3 ± 10.5 nm to 244.9 ± 6.0 nm causes an increase in capacitance, a further reduction to 204.0 ± 8.1 nm causes decreased capacitance. These results show that defect engineering is a powerful tool to improve the performance of supercapacitor materials, although careful tuning is required to ensure that defects do not end up being a hindrance.

Chapter 6: Conclusions and Future Work

6.1 Summary of Findings

By depositing densely tiled monolayers of MoS_2 on HOPG in aqueous and organic electrolyte, we measured, for the first time, the intrinsic capacitance of 1T and 2H MoS_2. The 1T and 2H MoS_2 polymorphs exhibited intrinsic capacitance values of 14.9 $\mu F/cm^2$ and 1.39 $\mu F/cm^2$, respectively, under negative polarization with little frequency dependence, demonstrating over tenfold difference. Over all potentials studied, the capacitance of the electrode/electrolyte interface is reduced when an organic electrolyte is used compared to an aqueous one. This can be explained by a decrease in the Helmholtz capacitance in organic electrolyte. An unexpected result is that the capacitance of the 1T MoS_2/electrolyte interface approaches that of the 2H phase under positive polarization. This suggests that positive polarization causes the 1T polymorph to become electronically similar to the semi-conducting 2H polymorph which is not readily explained and left to future work.

Multilayer MoS_2 was also investigated to explore the effects of restacking. The capacitance of multilayer MoS_2 films increased with each further monolayer deposition, suggesting that MoS_2 nanosheets restack in a way that does not reduce accessible surface area. As a point of comparison, multilayer rGO was also investigated. While a slight increase in capacitance between the first and second layer of rGO is observed, no further enhancement to the capacitance for subsequent layers occurs. This is because rGO aggregate and restack when layered on top of each other, reducing accessible surface area and decreasing overall capacitance.

The intrinsic capacitance was extrapolated from measured values and also calculated according to previously reported works. In order to determine which assumptions were most likely to be valid, measured values were compared with the calculated values. This analysis affirms that electrolyte ions can intercalate between adjacent MoS_2 layers and also between the MoS_2 and HOPG supporting electrode. Using these measured values, we extrapolate theoretical gravimetric and volumetric limits for supercapacitors comprised entirely from 1T MoS_2. The results suggest that these limits have already been reached and introducing defects or other materials or incorporating MoS_2 into the negative electrode of an asymmetric supercapacitor may be necessary to further improve the energy density of supercapacitors based on MoS_2.

In order to investigate the utility of defect engineering of MoS_2, two types of defects were introduced into MoS_2 nanosheets: sulfur vacancies and edge sites. Sulfur vacancies were introduced by increasing the amount of lithium intercalant used during exfoliation of bulk MoS_2 while edge sites were created by decreasing lateral flake size through probe sonication. The results showed that an increase in percentage of sulfur vacancies from 0.0% to 6.6% resulted in a continuous increase in capacitance. Conversely, while an initial reduction in flake size increased capacitance, further size reduction resulted in decreased capacitance. These results indicate that while defect engineering is a powerful tool for enhancement of capacitance, careful tuning is required to prevent the defects from having an adverse effect on capacitance.

6.2 Recommendations for Future Work

6.2.1 Limits of Defect Engineering

While a limit is observed to defect engineering of MoS_2 nanosheets through lateral flake size reduction, the same cannot be said for the introduction of sulfur vacancies. The relationship between percentage of sulfur vacancies and intrinsic capacitance appeared linear, as if increasing the ratio of n-butyllithium to bulk MoS_2 could ceaselessly improve capacitance. Logically, this should not be the case and a point at which this method of defect engineering proves ineffective must exist. It is unknown where this point lies, whether it requires five or fifty times the amount of intercalant used, or by how much the intrinsic capacitance can be enhanced through this method.

6.2.2 Effect of Oxygen Defects

Many articles have been published detailing hybrid supercapacitors made using MoS_2 and MoO_x.[32,92] Similarly, much research has been done on the improvement of other properties, such as catalytic performance or photoluminescence, through the introduction of oxygen defects.[79,80,93] MoO_x can very simply be introduced to MoS_2 in a somewhat controllable manner through exposure to ozone made by UV-light.[94-96] Therefore, it may be of interest to explore how defect engineering of MoS_2 through ozone exposure affects the intrinsic capacitance.

6.2.3 Defect Engineering and Cycle Stability

While defect engineering has been shown to be effective in increasing the intrinsic capacitance of monolayer MoS_2, it is uncertain how multilayer MoS_2, and more importantly, how actual supercapacitor devices made with MoS_2 would be affected by the defects. When one thinks

about defects, one also thinks about how the cycle stability may be affected. Thus, it may be worthwhile to compare the performance of supercapacitors made with pristine and defect engineered MoS_2, with particular focus on the cycle stability.

6.2.4 Intrinsic Capacitance of Other Materials

The research conducted in this thesis produced numerous insights on the nature of charge storage in MoS_2 nanosheets. Likewise, previous, similar studies on graphene resulted in an explanation to the once confounding problem of low measured capacitance. Great value exists in fundamental studies of other supercapacitor materials. For example, MXenes are a class of two-dimensional inorganic compounds which have also become prominently used in supercapacitor devices.[3,97,98] However, the intrinsic capacitance of MXenes is still unknown, and so its investigation may unearth useful knowledge for the fabrication of efficient supercapacitor devices.

Chapter 7: Bibliography

(1)   Theerthagiri, J.; Senthil, R. A.; Senthilkumar, B.; Reddy Polu, A.; Madhavan, J.; Ashokkumar, M. Recent Advances in MoS2 Nanostructured Materials for Energy and Environmental Applications – A Review. *J. Solid State Chem.* **2017**, *252*, 43–71.

(2)   Attanayake, N. H.; Thenuwara, A. C.; Patra, A.; Aulin, Y. V.; Tran, T. M.; Chakraborty, H.; Borguet, E.; Klein, M. L.; Perdew, J. P.; Strongin, D. R. Effect of Intercalated Metals on the Electrocatalytic Activity of 1T-MoS2 for the Hydrogen Evolution Reaction. *ACS Energy Lett.* **2018**, *3*, 7–13.

(3)   Kumar, K. S.; Choudhary, N.; Jung, Y.; Thomas, J. Recent Advances in Two-Dimensional Nanomaterials for Supercapacitor Electrode Applications. *ACS Energy Lett.* **2018**, *3*, 482–495.

(4)   Wang, T.; Chen, S.; Pang, H.; Xue, H.; Yu, Y. MoS2-Based Nanocomposites for Electrochemical Energy Storage. *Adv. Sci.* **2017**, *4*.

(5)   Rao, C. N. R.; Gopalakrishnan, K.; Maitra, U. Comparative Study of Potential Applications of Graphene, MoS2, and Other Two-Dimensional Materials in Energy Devices, Sensors, and Related Areas. *ACS Appl. Mater. Interfaces* **2015**, *7*, 7809–7832.

(6)   Wang, R.; Wang, S.; Jin, D.; Zhang, Y.; Cai, Y.; Ma, J.; Zhang, L. Engineering Layer Structure of MoS 2 -Graphene Composites with Robust and Fast Lithium Storage for High-Performance Li-Ion Capacitors. *Energy Storage Mater.* **2017**, *9*, 195–205.

(7)   Tang, H.; Wang, J.; Yin, H.; Zhao, H.; Wang, D.; Tang, Z. Growth of Polypyrrole Ultrathin Films on Mos2 Monolayers as High-Performance Supercapacitor Electrodes. *Adv. Mater.* **2015**, *27*, 1117–1123.

(8)   Simon, P.; Gogotsi, Y. Capacitive Energy Storage in Nanostructured Carbon-Electrolyte Systems. *Acc. Chem. Res.* **2013**, *46*, 1094–1103.

(9)   Helmholtz, H. Studien Über Electrische Grenzschichten. *Ann. der Phys. und Chemie* **1879**, *7*, 22.

(10)   Conway, B. E. *Electrochemical Supercapacitors: Scientific Fundamentals and Technological Applications*; New York, 1999.

(11)   Zhang, Y.; Feng, H.; Wu, X.; Wang, L.; Zhang, A.; Xia, T.; Dong, H.; Li, X.; Zhang, L. Progress of Electrochemical Capacitor Electrode Materials: A Review. *Int. J. Hydrogen Energy* **2009**, *34*, 4889–4899.

(12)   Nandi, D. K.; Sahoo, S.; Sinha, S.; Yeo, S.; Kim, H.; Bulakhe, R. N.; Heo, J.; Shim, J. J.; Kim, S. H. Highly Uniform Atomic Layer-Deposited MoS 2 @3D-Ni-Foam: A Novel Approach to Prepare an Electrode for Supercapacitors. *ACS Appl. Mater. Interfaces* **2017**, *9*, 40252–40264.

(13)   Acerce, M.; Voiry, D.; Chhowalla, M. Metallic 1T Phase MoS2 Nanosheets as Supercapacitor Electrode Materials. *Nat. Nanotechnol.* **2015**, *10*, 313–318.

(14)   Geim, A. K.; Novoselov, K. S. The Rise of Graphene. *Nat. Mater.* **2007**, *6*, 183–191.

(15)   Yin, Y.; Han, J.; Zhang, Y.; Zhang, X.; Xu, P.; Yuan, Q.; Samad, L.; Wang, X.; Wang, Y.; Zhang, Z.; Zhang, P.; Cao, X.; Song, B.; Jin, S. Contributions of Phase, Sulfur Vacancies, and Edges to the

Hydrogen Evolution Reaction Catalytic Activity of Porous Molybdenum Disulfide Nanosheets. *J. Am. Chem. Soc.* **2016**, *138*, 7965–7972.

(16) Xu, L.; Tetreault, A. R.; Khaligh, H. H.; Goldthorpe, I. A.; Wettig, S. D.; Pope, M. A. Continuous Langmuir-Blodgett Deposition and Transfer by Controlled Edge-to-Edge Assembly of Floating 2D Materials. *Langmuir* **2019**, *35*, 51–59.

(17) Zhang, Y.; Xu, L.; Walker, W. R.; Tittle, C. M.; Backhouse, C. J.; Pope, M. A. Langmuir Films and Uniform, Large Area, Transparent Coatings of Chemically Exfoliated MoS2 Single Layers. *J. Mater. Chem. C* **2017**, *5*, 11275–11287.

(18) Acerce, M.; Voiry, D.; Chhowalla, M. Metallic 1T Phase MoS2 Nanosheets as Supercapacitor Electrode Materials. *Nat. Nanotechnol.* **2015**, *10*, 313–318.

(19) Voiry, D.; Mohite, A.; Chhowalla, M. Phase Engineering of Transition Metal Dichalcogenides. *Chem. Soc. Rev.* **2015**, *44*, 2702–2712.

(20) Wypych, F.; Schöllhorn, R. 1T-MoS2, a New Metallic Modification of Molybdenum Disulfide. *J. Chem. Soc. Chem. Commun.* **1992**, No. 19, 1386–1388.

(21) Eda, G.; Yamaguchi, H.; Voiry, D.; Fujita, T.; Chen, M.; Chhowalla, M. Photoluminescence from Chemically Exfoliated MoS 2. *Nano Lett.* **2011**, *11*, 5111–5116.

(22) Sim, D. M.; Han, H. J.; Yim, S.; Choi, M. J.; Jeon, J.; Jung, Y. S. Long-Term Stable 2H-MoS2 Dispersion: Critical Role of Solvent for Simultaneous Phase Restoration and Surface Functionalization of Liquid-Exfoliated MoS 2. *ACS Omega* **2017**, *2*, 4678–4687.

(23) Wu, J.; Dai, J.; Shao, Y.; Cao, M.; Wu, X. Carbon Dot-Assisted Hydrothermal Synthesis of Flower-like MoS2 Nanospheres Constructed by Few-Layered Multiphase MoS2 Nanosheets for Supercapacitors. *RSC Adv.* **2016**, *6*, 77999–78007.

(24) Fang, L.; Qiu, Y.; Li, W.; Wang, F.; Lan, M.; Huang, K.; Jing, Q. Three-Dimensional Flower-like MoS2-CoSe2 Heterostructure for High Performance Superccapacitors. *J. Colloid Interface Sci.* **2018**, *512*, 282–290.

(25) Lingappan, N.; Van, N. H.; Lee, S.; Kang, D. J. Growth of Three Dimensional Flower-like Molybdenum Disulfide Hierarchical Structures on Graphene/Carbon Nanotube Network: An Advanced Heterostructure for Energy Storage Devices. *J. Power Sources* **2015**, *280*, 39–46.

(26) Chen, M.; Wang, J.; Yan, X.; Ren, J.; Dai, Y.; Wang, Q.; Wang, Y.; Cheng, X. Flower-like Molybdenum Disulfide Nanosheets Grown on Carbon Nanosheets to Form Nanocomposites: Novel Structure and Excellent Electrochemical Performance. *J. Alloys Compd.* **2017**, *722*, 250–258.

(27) Ilanchezhiyan, P.; Mohan Kumar, G.; Kang, T. W. Electrochemical Studies of Spherically Clustered MoS2 Nanostructures for Electrode Applications. *J. Alloys Compd.* **2015**, *634*, 104–108.

(28) Lin, T. W.; Hsiao, M. C.; Wang, A. Y.; Lin, J. Y. Hollow Hierarchical Carbon Spheres Decorated with Ultrathin Molybdenum Disulfide Nanosheets as High-Capacity Electrode Materials for Asymmetric Supercapacitors. *ChemElectroChem* **2017**, *4*, 620–627.

(29) Kamila, S.; Mohanty, B.; Samantara, A. K.; Guha, P.; Ghosh, A.; Jena, B.; Satyam, P. V.; Mishra, B.

K.; Jena, B. K. Highly Active 2D Layered MoS2-RGO Hybrids for Energy Conversion and Storage Applications. *Sci. Rep.* **2017**, *7*, 1–13.

(30)   Nandi, D. K.; Sahoo, S.; Sinha, S.; Yeo, S.; Kim, H.; Bulakhe, R. N.; Heo, J.; Shim, J. J.; Kim, S. H. Highly Uniform Atomic Layer-Deposited MoS2@3D-Ni-Foam: A Novel Approach to Prepare an Electrode for Supercapacitors. *ACS Appl. Mater. Interfaces* **2017**, *9*, 40252–40264.

(31)   Balasingam, S. K.; Lee, M.; Kim, B. H.; Lee, J. S.; Jun, Y. Freeze-Dried MoS2 Sponge Electrodes for Enhanced Electrochemical Energy Storage. *Dalt. Trans.* **2017**, *46*, 2122–2128.

(32)   Zhang, T.; Kong, L. Bin; Liu, M. C.; Dai, Y. H.; Yan, K.; Hu, B.; Luo, Y. C.; Kang, L. Design and Preparation of MoO2/MoS2 as Negative Electrode Materials for Supercapacitors. *Mater. Des.* **2016**, *112*, 88–96.

(33)   Chen, Y.; Ma, W.; Cai, K.; Yang, X.; Huang, C. In Situ Growth of Polypyrrole onto Three-Dimensional Tubular MoS2 as an Advanced Negative Electrode Material for Supercapacitor. *Electrochim. Acta* **2017**, *246*, 615–624.

(34)   Lamberti, A. Flexible Supercapacitor Electrodes Based on MoS2-Intercalated RGO Membranes on Ti Mesh. *Mater. Sci. Semicond. Process.* **2018**, *73*, 106–110.

(35)   Zhang, H.; Qin, G.; Lin, Y.; Zhang, D.; Liao, H.; Li, Z.; Tian, J.; Wu, Q. A Novel Flexible Electrode with Coaxial Sandwich Structure Based Polyaniline-Coated MoS2 Nanoflakes on Activated Carbon Cloth. *Electrochim. Acta* **2018**, *264*, 91–100.

(36)   Wang, J.; Wu, Z.; Hu, K.; Chen, X.; Yin, H. High Conductivity Graphene-like MoS 2 /Polyaniline Nanocomposites and Its Application in Supercapacitor. *J. Alloys Compd.* **2015**, *619*, 38–43.

(37)   She, Z.; Ghosh, D.; Pope, M. A. Decorating Graphene Oxide with Ionic Liquid Nanodroplets: An Approach Leading to Energy-Dense, High-Voltage Supercapacitors. *ACS Nano* **2017**, *11*, 10077–10087.

(38)   Pope, M. A.; Punckt, C.; Aksay, I. A. Intrinsic Capacitance and Redox Activity of Functionalized Graphene Sheets. *J. Phys. Chem. C* **2011**, *115*, 20326–20334.

(39)   Xia, J.; Chen, F.; Li, J.; Tao, N. Measurement of the Quantum Capacitance of Graphene. *Nat. Nanotechnol.* **2009**, *4*, 505–509.

(40)   Fang, T.; Konar, A.; Xing, H.; Jena, D. Carrier Statistics and Quantum Capacitance of Graphene Sheets and Ribbons. *Appl. Phys. Lett.* **2007**, *91*, 2007–2009.

(41)   Stoller, M. D.; Magnuson, C. W.; Zhu, Y.; Murali, S.; Suk, J. W.; Piner, R.; Ruoff, R. S. Interfacial Capacitance of Single Layer Graphene. *Energy Environ. Sci.* **2011**, *4*, 4685–4689.

(42)   Pope, M. A.; Aksay, I. A. Four-Fold Increase in the Intrinsic Capacitance of Graphene through Functionalization and Lattice Disorder. *J. Phys. Chem. C* **2015**, *119*, 20369–20378.

(43)   Randin, J.-P.; Yeager, E. Differential Capacitance Study on the Basal Plane of Stress-Annealed Pyrolytic Graphite. *J. Electroanal. Chem. Interfacial Electrochem.* **1972**, *36*, 257.

(44)   Randin, J.-P.; Yeager, E. Differential Capacitance Study on the Edge Orientation of Pyrolytic Graphite and Glassy Carbon Electrodes. *J. Electroanal. Chem. Interfacial Electrochem.* **1975**, *58*, 313–

322.

(45)   Gerischer, H. An Interpretation of the Double Layer Capacity of Graphite Electrodes in Relation to the Density of States at the Fermi Level. *J. Phys. Chem.* **1985**, *89*, 4249–4251.

(46)   Paek, E.; Pak, A. J.; Hwang, G. S. A Computational Study of the Interfacial Structure and Capacitance of Graphene in [BMIM][PF6] Ionic Liquid. *J. Electrochem. Soc.* **2012**, *160*, A1–A10.

(47)   Pak, A. J.; Hwang, G. S. Molecular Insights into the Complex Relationship between Capacitance and Pore Morphology in Nanoporous Carbon-Based Supercapacitors. *ACS Appl. Mater. Interfaces* **2016**, *8*, 34659–34667.

(48)   Wang, J.; Deng, S.; Liu, Z.; Liu, Z. The Rare Two-Dimensional Materials with Dirac Cones. *Natl. Sci. Rev.* **2015**, *2*, 22–39.

(49)   Goh, M. S.; Pumera, M. Multilayer Graphene Nanoribbons Exhibit Larger Capacitance than Their Few-Layer and Single-Layer Graphene Counterparts. *Electrochem. commun.* **2010**, *12*, 1375–1377.

(50)   Pope, M. A. Electrochemical Double-Layer Capacitors Based of Functionalized Graphene. **2013**.

(51)   Roberts, G. G. An Applied Science Perspective of Langmuir-Blodgett Films. *Adv. Phys.* **1985**, *34*, 475–512.

(52)   Pockels, A. On the Relative Contamination of the Water-Surface by Equal Quantities of Different Substances. *Nature* **1892**, *46*.

(53)   Pockels, A.; Rayleigh, Lord. Surface Tension. *Nature* **1891**, *43*.

(54)   Langmuir, I. The Constitution and Fundamental Properties of Solids and Liquids. Part I. Solids. *J. Am. Chem. Soc.* **1916**, *38*, 2221–2295.

(55)   Wales, D. J.; Kitchen, J. A. Surface-Based Molecular Self-Assembly: Langmuir-Blodgett Films of Amphiphilic Ln(III) Complexes. *Chem. Cent. J.* **2016**, *10*, 1–8.

(56)   Yoon, Y.; Ganapathi, K.; Salahuddin, S. How Good Can Monolayer MoS2 Transistors Be? *Nano Lett.* **2011**, *11*, 3768–3773.

(57)   Chen, J.; Walker, W. R.; Xu, L.; Krysiak, O.; She, Z.; Pope, M. Intrinsic Capacitance of Molybdenum Disulfide. *ACS Nano* **2020**.

(58)   Hummers, W. S.; Offeman, R. E. Preparation of Graphitic Oxide. *J. Am. Chem. Soc.* **1958**, *80*, 1339.

(59)   Marcano, D. C.; Kosynkin, D. V.; Berlin, J. M.; Sinitskii, A.; Sun, Z.; Slesarev, A.; Alemany, L. B.; Lu, W.; Tour, J. M. Improved Synthesis of Graphene Oxide. *ACS Nano* **2010**, *4*, 4806–4814.

(60)   Park, S.; An, J.; Jung, I.; Piner, R. D.; An, S. J.; Li, X.; Velamakanni, A.; Ruoff, R. S. Colloidal Suspensions of Highly Reduced Graphene Oxide in a Wide Variety of Organic Solvents. *Nano Lett.* **2009**, *9*, 1593–1597.

(61)   Papageorgopoulos, C. A.; Jaegermann, W. Li Intercalation across and along the van Der Waals Surfaces of MoS2 (0001). *Surf. Sci.* **1995**, *338*, 83–93.

(62)   Knirsch, K. C.; Berner, N. C.; Nerl, H. C.; Cucinotta, C. S.; Gholamvand, Z.; McEvoy, N.; Wang, Z.; Abramovic, I.; Vecera, P.; Halik, M.; Sanvito, S.; Duesberg, G. S.; Nicolosi, V.; Hauke, F.; Hirsch,

A.; Coleman, J. N.; Backes, C. Basal-Plane Functionalization of Chemically-Exfoliated Molybdenum Disulfide by Diazonium Salts. *ACS Nano* **2015**, 1–41.

(63)   Xu, L.; Tetreault, A. R.; Pope, M. A. Chemical Insights into the Rapid, Light-Induced Auto-Oxidation of Molybdenum Disulfide Aqueous Dispersions. *Chem. Mater.* **2020**, *32*, 148–156.

(64)   Ambrosi, A.; Sofer, Z.; Pumera, M. 2H → 1T Phase Transition and Hydrogen Evolution Activity of MoS2, MoSe2, WS2 and WSe2 Strongly Depends on the MX2 Composition. *Chem. Commun.* **2015**, *51*, 8450–8453.

(65)   Fan, X.; Xu, P.; Zhou, D.; Sun, Y.; Li, Y. C.; Nguyen, M. A. T.; Terrones, M.; Mallouk, T. E. Fast and Efficient Preparation of Exfoliated 2H MoS2 Nanosheets by Sonication-Assisted Lithium Intercalation and Infrared Laser-Induced 1T to 2H Phase Reversion. *Nano Lett.* **2015**, *15*, 5956–5960.

(66)   Sun, Z.; Zhao, Q.; Zhang, G.; Li, Y.; Zhang, G.; Zhang, F.; Fan, X. Exfoliated MoS2 Supported Au-Pd Bimetallic Nanoparticles with Core-Shell Structures and Superior Peroxidase-like Activities. *RSC Adv.* **2015**, *5*, 10352–10357.

(67)   Luxa, J.; Jankovský, O.; Sedmidubský, D.; Medlín, R.; Maryško, M.; Pumera, M.; Sofer, Z. Origin of Exotic Ferromagnetic Behavior in Exfoliated Layered Transition Metal Dichalcogenides MoS2 and WS2. *Nanoscale* **2016**, *8*, 1960–1967.

(68)   Chacko, L.; Rastogi, P. K.; Aneesh, P. M. Phase Engineering from 2H to 1T-MoS 2 for Efficient Ammonia PL Sensor and Electrocatalyst for Hydrogen Evolution Reaction . *J. Electrochem. Soc.* **2019**, *166*, H263–H271.

(69)   Knirsch, K. C.; Berner, N. C.; Nerl, H. C.; Cucinotta, C. S.; Gholamvand, Z.; McEvoy, N.; Wang, Z.; Abramovic, I.; Vecera, P.; Halik, M.; Sanvito, S.; Duesberg, G. S.; Nicolosi, V.; Hauke, F.; Hirsch, A.; Coleman, J. N.; Backes, C. Basal-Plane Functionalization of Chemically Exfoliated Molybdenum Disulfide by Diazonium Salts. *ACS Nano* **2015**, *9*, 6018–6030.

(70)   Fan, X.; Xu, P.; Li, Y. C.; Zhou, D.; Sun, Y.; Nguyen, M. A. T.; Terrones, M.; Mallouk, T. E. Controlled Exfoliation of MoS2 Crystals into Trilayer Nanosheets. *J. Am. Chem. Soc.* **2016**, *138*, 5143–5149.

(71)   Lembke, D.; Kis, A. Breakdown of High-Performance Monolayer MoS2 Transistors. *ACS Nano* **2012**, *6*, 10070–10075.

(72)   Nair, R. R.; Blake, P.; Grigorenko, A. N.; Novoselov, K. S.; Booth, T. J.; Stauber, T.; Peres, N. M. R.; Geim, A. K. Fine Structure Constant Defines Visual Transparency of Graphene. *Science (80-.).* **2008**, *320*, 1308–1308.

(73)   Qu, D.; Shi, H. Studies of Activated Carbons Used in Double-Layer Capacitors. *J. Power Sources* **1998**, *74*, 99–107.

(74)   Aldama, I.; Barranco, V.; Kunowsky, M.; Ibañez, J.; Rojo, J. M. Contribution of Cations and Anions of Aqueous Electrolytes to the Charge Stored at the Electric Electrolyte/Electrode Interface of Carbon-Based Supercapacitors. *J. Phys. Chem. C* **2017**, *121*, 12053–12062.

(75)   Kemp, D. D.; Gordon, M. S. Theoretical Study of the Solvation of Fluorine and Chlorine Anions by

Water. *J. Phys. Chem. A* **2005**, *109*, 7688–7699.

(76)   Mamardashvili, G. M.; Mamardashvili, N. Z.; Koifman, O. I. Synthesis and Receptor Properties of Calix[4]Pyrroles. *Russ. Chem. Rev.* **2015**, *84*, 275–287.

(77)   Nightingale, E. R. Phenomenological Theory of Ion Solvation. Effective Radii of Hydrated Ions. *J. Phys. Chem.* **1959**, *63*, 1381–1387.

(78)   Marcus, Y. A Simple Empirical Model Describing the Thermodynamics of Hydration of Ions of Widely Varying Charges, Sizes, and Shapes. *Biophys. Chem.* **1994**, *51*, 111–127.

(79)   Sun, T.; Li, Z.; Liu, X.; Ma, L.; Wang, J.; Yang, S. Oxygen-Incorporated MoS2 Microspheres with Tunable Interiors as Novel Electrode Materials for Supercapacitors. *J. Power Sources* **2017**, *352*, 135–142.

(80)   Zhou, J.; Fang, G.; Pan, A.; Liang, S. Oxygen-Incorporated MoS2 Nanosheets with Expanded Interlayers for Hydrogen Evolution Reaction and Pseudocapacitor Applications. *ACS Appl. Mater. Interfaces* **2016**, *8*, 33681–33689.

(81)   Anand, H.; Verma, R. Solvation of Some Tetraalkylammonium Salts Investigated Conductometrically and Viscometrically in Binary Mixtures of Acetonitrile + Methanol at 298.15 K. *Zeitschrift fur Phys. Chemie* **2016**, *230*, 1759–1772.

(82)   Huang, H.; Li, Z.; She, J.; Wang, W. Oxygen Density Dependent Band Gap of Reduced Graphene Oxide. *J. Appl. Phys.* **2012**, *111*.

(83)   Davelou, D.; Kopidakis, G.; Kioseoglou, G.; Remediakis, I. N. MoS2 Nanostructures: Semiconductors with Metallic Edges. *Solid State Commun.* **2014**, *192*, 42–46.

(84)   Gerischer, H. Advances in Electrochemistry and Electrochemical Engineering. *Intersci. Publ.* **1961**, *1*, 155.

(85)   Lee, S. K.; Chu, D.; Song, D. Y.; Pak, S. W.; Kim, E. K. Electrical and Photovoltaic Properties of Residue-Free MoS2 Thin Films by Liquid Exfoliation Method. *Nanotechnology* **2017**, *28*, 195703.

(86)   Wang, K. C.; Stanev, T. K.; Valencia, D.; Charles, J.; Henning, A.; Sangwan, V. K.; Lahiri, A.; Mejia, D.; Sarangapani, P.; Povolotskyi, M.; Afzalian, A.; Maassen, J.; Klimeck, G.; Hersam, M. C.; Lauhon, L. J.; Stern, N. P.; Kubis, T. Control of Interlayer Physics in 2H Transition Metal Dichalcogenides. *J. Appl. Phys.* **2017**, *122*, 224302.

(87)   Hou, Y.; Aoki, K. J.; Chen, J.; Nishiumi, T. Solvent Variables Controlling Electric Double Layer Capacitance at the Metal-Solution Interface. *J. Phys. Chem. C* **2014**, *118*, 10153–10158.

(88)   Worsley, M. A.; Shin, S. J.; Merrill, M. D.; Lenhardt, J.; Nelson, A. J.; Woo, L. Y.; Gash, A. E.; Baumann, T. F.; Orme, C. A. Ultralow Density, Monolithic WS2, MoS2, and MoS2/Graphene Aerogels. *ACS Nano* **2015**, *9*, 4698–4705.

(89)   Chhowalla, M.; Shin, H. S.; Eda, G.; Li, L. J.; Loh, K. P.; Zhang, H. The Chemistry of Two-Dimensional Layered Transition Metal Dichalcogenide Nanosheets. *Nat. Chem.* **2013**, *5*, 263–275.

(90)   Mignuzzi, S.; Pollard, A. J.; Bonini, N.; Brennan, B.; Gilmore, I. S.; Pimenta, M. A.; Richards, D.; Roy, D. Effect of Disorder on Raman Scattering of Single-Layer Mo S2. *Phys. Rev. B - Condens.*

Matter Mater. Phys. **2015**, *91*, 1–7.

(91)   Abdelaziz Aboelazm, E. A.; Mohammed Ali, G. A.; Algarni, H.; Chong, K. F. Flakes Size-Dependent Optical and Electrochemical Properties of MoS2. *Curr. Nanosci.* **2018**, *14*, 416–420.

(92)   Yin, Z.; Zhang, X.; Cai, Y.; Chen, J.; Wong, J. I.; Tay, Y. Y.; Chai, J.; Wu, J.; Zeng, Z.; Zheng, B.; Yang, H. Y.; Zhang, H. Preparation of MoS2-MoO3 Hybrid Nanomaterials for Light-Emitting Diodes. *Angew. Chemie - Int. Ed.* **2014**, *53*, 12560–12565.

(93)   Nan, H.; Wang, Z.; Wang, W.; Liang, Z.; Lu, Y.; Chen, Q.; He, D.; Tan, P.; Miao, F.; Wang, X.; Wang, J.; Ni, Z. Strong Photoluminescence Enhancement of MoS2 through Defect Engineering and Oxygen Bonding. *ACS Nano* **2014**, *8*, 5738–5745.

(94)   Qin, P.; Fang, G.; Ke, W.; Cheng, F.; Zheng, Q.; Wan, J.; Lei, H.; Zhao, X. In Situ Growth of Double-Layer MoO3/MoS2 Film from MoS2 for Hole-Transport Layers in Organic Solar Cell. *J. Mater. Chem. A* **2014**, *2*, 2742–2756.

(95)   Su, W.; Kumar, N.; Spencer, S. J.; Dai, N.; Roy, D. Transforming Bilayer MoS2 into Single-Layer with Strong Photoluminescence Using UV-Ozone Oxidation. *Nano Res.* **2015**, *8*, 3878–3886.

(96)   Burman, D.; Ghosh, R.; Santra, S.; Ray, S. K.; Guha, P. K. Role of Vacancy Sites and UV-Ozone Treatment on Few Layered MoS2 Nanoflakes for Toxic Gas Detection. *Nanotechnology* **2017**, *28*, 1–5.

(97)   Navarro-Suárez, A. M.; Maleski, K.; Makaryan, T.; Yan, J.; Anasori, B.; Gogotsi, Y. 2D Titanium Carbide/Reduced Graphene Oxide Heterostructures for Supercapacitor Applications. *Batter. Supercaps* **2018**, *1*, 33–38.

(98)   Yan, J.; Ren, C. E.; Maleski, K.; Hatter, C. B.; Anasori, B.; Urbankowski, P.; Sarycheva, A.; Gogotsi, Y. Flexible MXene/Graphene Films for Ultrafast Supercapacitors with Outstanding Volumetric Capacitance. *Adv. Funct. Mater.* **2017**, *27*, 1–10.